THE ROLE OF ADSORBED PHASE VOLUME ON THE THERMODYNAMICS OF SUPERCRITICAL METHANE ADSORPTION ON MICROPOROUS CARBON

by

Emily Lynn Remington

A thesis submitted in partial fulfillment
of the requirements for the degree

of

Master of Science

in

Mechanical Engineering

MONTANA STATE UNIVERSITY
Bozeman, Montana

April 2019

©COPYRIGHT

by

Emily Lynn Remington

2019

All Rights Reserved

ACKNOWLEDGEMENTS

There are several professors who taught me the fundamental knowledge that was required for me to confidently fulfill my graduate thesis work. These professors span across many disciplines including mechanical engineering, materials science, chemical engineering, and analytical chemistry. I have much appreciation for Dr. Sarah Codd who has been an empowering mentor and has encouraged me to pursue a degree in mechanical engineering. Dr. Stephen Sofie has been crucial for introducing me to the world of materials science; for me this ensured a fruitful transition from a career in architecture to mechanical engineering with an emphasis on materials engineering. I would also like to thank Dr. Paul Gannon for providing crucial guidance and for giving me a laboratory to participate in undergraduate and graduate research. Dr. Nicolas Stadie has been a major influence in growing my scientific understanding of complex systems. I am grateful for the summer project he allowed me to work on which flourished into my Master's thesis. This work has allowed me to reach a career goal of applying my mathematical background to experimental data to further the research and development of renewable energy technologies.

My parents, have also been a great support by inspiring me to strive for higher achievement. Without the support of my parents my extended family and my in-laws I would never have been able to make it to where I am. Finally, I would like to thank my husband for teaching me a work-life balance that I thrived upon to earn this degree.

TABLE OF CONTENTS

1. INTRODUCTION 1

1.1 Porous Carbon Materials 1
1.2 Adsorption Measurements 4
1.3 Adsorption Thermodynamics 7

2. METHODS 13

2.1 Experimental Methods 13
2.2 Data Analysis 14
2.3 Adsorbed Phase Volume Growth 16
2.4 Adsorption Equilibrium Models 18
2.5 Isosteric Heat of Adsorption 21
2.6 Helium Adsorption Correction 22
2.7 Isoexcess Heat of Adsorption 24

3. RESULTS 29

3.1 Goodness of Fit Criteria 29
3.2 Fitting of Uncorrected Methane Adsorption on CNS-201 30
3.3 Fitting of Helium Adsorption Corrected Methane Adsorption on CNS-201 31
3.4 Isosteric Heat of Adsorption of Methane on CNS-201 32
3.5 Isosteric Heat of Adsorption of Methane on MSC-30 and ZTC 34
3.6 Isoexcess Heat of Adsorption of Methane on CNS-201 34

4. DISCUSSION 48

5. CONCLUSIONS AND FUTURE WORK 54

REFERENCES CITED 56

APPENDIX 62

LIST OF TABLES

Table Page

1. Adsorption model nomenclature 26

2. Best fit parameter values and figure of assessment for CNS-201 based on raw experimental data 35

3. Best fit parameter values and figure of assessment for CNS-201 after helium correction 37

4. Best fit parameter values and figure of assessment for CNS-201 for isoexcess heat of adsorption calculation 44

LIST OF FIGURES

Figure Page

1. Carbide-derived carbon synthesized via halogenation 11

2. Synthesis procedure for zeolite-templated carbons 11

3. “Delivered fraction” of adsorptive characterized by different distributions of adsorption sites 12

4. Adsorbed phase volume growth models 27

5. Global best fit results of uncorrected excess adsorption equilibria 39

6. Global best fit results of helium corrected excess adsorption equilibria 40

7. Fitted excess adsorption uptake and calculated isosteric heat of adsorption for CNS-201 at 247 K, 298 K, and 526 K 41

8. Fitted excess adsorption uptake and calculated isosteric heat of adsorption for MSC-30 and ZTC at 298 K 42

9. Fitted excess adsorption uptake and calculated isoexcess heat of adsorption for CNS-201 at 298 K before and after helium correction 43

NOMENCLATURE

Symbol	Description	Default Unit
A	Arrhenius constant	MPa^{-1}
E	energy of adsorption	$kJ\ mol^{-1}$
E_{min}	minimum adsorption energy	$kJ\ mol^{-1}$
E_{max}	maximum adsorption energy	$kJ\ mol^{-1}$
H_a	enthalpy of adsorbed phase	$mL\ mmol^{-1}$
H_g	enthalpy of gas phase	$mL\ mmol^{-1}$
K	equilibrium constant	MPa^{-1}
K_{growth}	Langmuir equilibrium constant	MPa^{-1}
K_{He}	Henry's Law equilibrium constant	MPa^{-1}
m	Sips heterogenous factor	-
n_a	absolute adsorbed amount	$mmol\ g^{-1}$
n_e	model excess adsorbed amount	$mmol\ g^{-1}$
$n_e{}^*$	measured excess adsorbed amount	$mmol\ g^{-1}$
$\bar{n}_e{}^*$	average measured excess adsorbed amount	$mmol\ g^{-1}$
n_{max}	number of adsorption sites	$mmol\ g^{-1}$
N	number of independent fitting parameters	-
P	pressure	MPa
P_c	critical pressure	MPa
q_{st}	isosteric heat of adsorption	$mL\ mmol^{-1}$
R	gas constant	$kJ\ K^{-1}\ mol^{-1}$
R^2	coefficient of determination	-
$R^2{}_a$	adjusted coefficient of determination	-
t	Tóth heterogenous factor	-
T	temperature	K
T_c	critical temperature	K
V_a	volume of adsorbed phase	$mL\ g^{-1}$
V_{max}	volume at maximum adsorption	$mL\ g^{-1}$
α	weight factor	-
θ	fractional adsorbed amount	-
θ_{growth}	single-site Langmuir fractional adsorbed amount	-
ν_a	molar volume of adsorbed phase	$mL\ mmol^{-1}$
ν_g	molar volume of bulk phase	$mL\ mmol^{-1}$
ρ_a	density of adsorbed phase	$mmol\ L^{-1}$
ρ_g	density of bulk phase	$mL\ mmol^{-1}$
ΔH_{ads}	differential enthalpy of adsorption	$mL\ mmol^{-1}$
ΔS	differential entropy	R
ΔS_{ads}	differential entropy of adsorption	$J\ K^{-1}$
ΔU_{ads}	differential binding energy of adsorption	kJ
$\Delta \nu_{ads}$	differential specific volume of adsorption layer	$mL\ g^{-1}$

ABSTRACT

Experimental determination of the isosteric heat of adsorption at the fluid-solid interface is an important undertaking in the chemical sciences since this fundamental thermodynamic quantity is closely related to the binding energy of the adsorbate on the adsorbent surface. The usual methods employed to calculate the isosteric heat from measured gas adsorption equilibria, however, are unsuited to the treatment of adsorption under a high-pressure adsorptive fluid (where the difference in molar volume between the two phases becomes small and depends significantly on that of the adsorbed phase). Herein we employ a methodological approach to the thermodynamic analysis of adsorption up to high pressures in the supercritical regime, with a specific focus on methane adsorption on microporous carbonaceous materials at T/T_c between 1.25-2.75 and P/P_c up to 2. The aim is to achieve a meritorious description of the thermodynamics of the adsorbed phase with as few independent parameters as possible. We compare several simple approaches to estimating the molar volume of the adsorbed phase, and demonstrate that among the several well-known sources of error involved in the isosteric approach, that attributed to molar volume estimations is not itself prohibitive to achieving meritorious results. We contrast the isosteric approach with that of the so-called "isoexcess" methodology, and thereby shed new insights into the key role of the finite adsorbed phase volume in assessments of adsorption thermodynamics.

CHAPTER ONE

INTRODUCTION

1.1 Porous Carbon Materials

Porous carbons are an attractive class of materials for various applications including fluid purification,[1] electrochemical energy storage,[2] and gas storage and separation.[3] The desired pore shape and size differs depending on the application of interest. The International Union of Pure and Applied Chemistry (IUPAC) classifies pore size as microporous (< 2nm), mesoporous (2 nm – 50 nm), and macroporous (> 50 nm), loosely based on the phenomenon of capillary condensation of small molecular guests.[4] While mesopores are essential for biofluid purification, most ion and gas storage applications benefit most from microporous structures.[5] In hydrogen storage, for example, the optimal pore diameter is 0.6-0.7 nm when the operating conditions are at 77 K (liquid nitrogen temperature) and elevated pressures.[6] Similarly, 0.8-1.5 nm slit-shaped pores have been determined as the ideal pore width for methane storage at ambient temperature.[7] Historically, a major challenge in employing porous carbons for high-precision separations or high-performance energy storage has been in achieving uniform pore sizes through traditional synthesis techniques, including by physical or chemical activation, catalytic activation, or carbonatization of polymers.

Recent strategies to improve the uniformity of these materials have proven to be successful.[8] Carbide-derived carbons (CDCs) and zeolite templated carbons

(ZTCs) are two classes of porous carbon materials whose synthesis techniques were investigated as viable solutions for achieving structures with controlled pore size(s).[5, 8] Similar structures to CDCs and ZTCs with microporous frameworks, such as activated carbon, are typically disordered with clumped and/or stacked graphenes.[9] However, traditional synthesis techniques can also, under certain serendipitous conditions, yield materials with a relatively narrow distribution of pore sizes. Coconut shell activated carbons (e.g., CNS-201 produced by A. C. Carbone Inc., Canada) are one such example, typically containing a majority of pores below 1 nm in width. CDCs and ZTCs have the added advantage of having highly tunable synthesis conditions (as in N-doping, for example). The advantage of ordered arrays of micropores is that this framework enables mass transport and can be used as a molecular sieve for various applications.

CDCs are derived from a metal carbide (MeC) precursor where chlorine (Cl_2) or a halogen containing gas is typically used as an etchant to selectively remove metal atoms from the lattice of the MeC at elevated temperatures, as shown in Figure 1.[10] As the metal atoms react with the etchant, a metal chloride species is formed that rapidly evaporates and leaves the carbide precursor, leaving behind a porous layer of carbon on the remaining metal carbide particles. This surface layer grows according to a core-shell model, where suitable processing conditions and duration result in a carbide core fully converted to porous carbon.[11] The pore size(s) and pore size distribution depend on the originating carbide precursor as the MeC acts as the template for the resulting CDC. Metal carbides with a cubic

structure tend to yield CDCs with a narrow pore size distribution compared to those derived from MeCs with rhombohedral or orthorhombic structures.[5] Structural uniformity is aided by the proximity of the neighboring carbon atoms once the metal has been selectively etched away, allowing the original volume and shape of the MeC precursor to be maintained. However, some degree of relaxation or recombination occurs and the pore size of the resulting materials is also controlled on a sub-nanometer level by the processing temperature; an increase in pore size is associated with an increase in processing temperature. Therefore, tunability of the microstructure and porosity of CDCs can be achieved by varying the metal carbide precursor and its morphological form, the synthesis technique, and several processing parameters.[5]

Beyond halogenation, additional synthesis routes to CDCs include vacuum decomposition, hydrothermal treatment, and thermal decomposition. Nevertheless, halogenation remains the most common route to CDCs,[12] despite several technical complexities. Although procedures for the safe handling of halogen and halogen-containing gases have been established on the industrial scale, Cl_2 and HCl are both toxic and highly corrosive which present health and safety risks as well as increased operation expenses. An inexpensive and relatively safe alternative halogenation reagent, ammonium chloride (NH_4Cl), was investigated herein. The preliminary results of this work have been presented elsewhere,[13] and further work is ongoing.

Zeolite-templated carbons (ZTCs) are a class of highly ordered microporous carbons made up by a 3D covalent network consisting of two-sided graphene sheets that are curved.[9] ZTCs have an extremely high surface area (>3500 $m^2 g^{-1}$) and a pore size of ~1.2 nm. The local bonding is amorphous while pore-to-pore order is ensured by the zeolite template. Structural regularity is only achieved when meticulous care is taken during synthesis to create a connected structure free of stacked layers of graphitic material.[9] The synthesis route[14] used to create ZTCs with ordered networks is shown in Figure 2. A zeolite with suitably large channels for carbon deposition is dried and then impregnated with a liquid hydrocarbon precursor (e.g., furfuryl alcohol). The initial hydrocarbon framework is then polymerized within the zeolite channels at relatively low temperature (e.g., 423 K). This framework is pyrolyzed at high temperature (e.g., 973 K) to remove hydrogen. The remaining voids in the formed carbon network are filled by a small hydrocarbon precursor under chemical vapor deposition (CVD) conditions, the composite material is heat-treated at 1173 K, and then cooled. Finally, the zeolite is dissolved using an acid treatment, resulting in a carbonaceous material (ZTC) with an ordered array of micropores.

1.2 Adsorption Measurements

Most carbonaceous materials have pore sizes ranging from micro- to macropores, and the appropriate technique(s) used to determine their pore size distribution is dependent on the size scale. For example, an optical microscope can

be used to identify macropores, while a scanning electron microscope (SEM) can detect pore sizes that range from mesopores to macropores. Gas adsorption, on the other hand, is the most common technique used to characterize materials with pore sizes ranging from micropores (~0.4 nm) to mesopores (~50 nm).[15]

There are two main types of adsorption measurement techniques: gravimetric and volumetric. The work described herein is based on volumetric adsorption measurements. For volumetric gas adsorption measurements, the real gas law is used to determine how much gas (adsorbate) is adsorbed by the sample (adsorbent) through a stepwise process. Before an adsorption measurement can take place, the sample must be degassed of any contaminant that had been adsorbed during the synthesis process or storage. The IUPAC has set guidelines for determining when a sample has been reasonably degassed which they specify as a pressure reading of 10 mPa after the sample cell has been exposed to vacuum. Therefore, the adsorption measurement starts at vacuum where the sample cell is isolated from a chamber containing a precise volume for dosing gas (adsorptive). The adsorptive is introduced into the calibrated dosing volume until a predetermined pressure has been reached. This precise quantity of adsorptive is then introduced into the sample cell where ample time is allotted to ensure that the pressure has reached equilibrium. The quantity adsorbed is determined by the additional pressure drop that is observed after the reduced pressure due purely to gas expansion has been accounted for. It is important to note that the quantity being measured is the excess adsorbed amount rather than an absolute amount of the

adsorbate. Once the first measurement has been recorded, the sample cell is isolated once again, the pressure of the adsorptive is increased in the dosing volume, and the process is repeated for numerous higher pressures until an isotherm has been obtained.

There are several sources of error that can impact the results of adsorption measurements. Calibration of the dosing volume and the temperature and pressure measurement devices are crucial for volumetric instruments. More specifically, with the adsorbed quantity for volumetric analyses requiring a summation over a range of pressures for a given isotherm, small errors incurred from a poorly calibrated pressure transducer would result in accumulated error. Similar errors will occur if the assumption of an isothermal dosing volume or sample were invalid, as the adsorbed quantity is dependent on the premise of knowing the adsorptive density in all parts of the apparatus. Another instrumental source of error that is a common cause for concern is a leak. To assess this source of error, the leak rate of a volumetric apparatus can be determined at the completion of measurement and used to qualify or disqualify the collected data.

In addition to instrumental sources of error, experimental errors may also occur. Sample size, gas purity, and sample degassing must be controlled to within acceptable specifications before adsorption measurements are taken. The size of the sample that is appropriate depends on the accuracy of the pressure transducer and the inner volumes of the system. It should be noted that a smaller mass might be adequate if the sample has a large adsorption capacity and vice versa for low

capacity materials. Ideally, the highest level of purity should be used for the gas being supplied for the sorption measurements. Any impurities in the gas may be adsorbed preferentially onto the sample and contribute error to the results. Finally, if the sample is not effectively degassed before the experiment begins, any pre-adsorbed gas from synthesis or storage will impact the resulting measurements, resulting in lower measured quantities than for a properly degassed sample.[16]

1.3 Adsorption Thermodynamics

The binding strength of an adsorbing fluid with respect to an adsorbent surface dominates the thermodynamics of a solid-fluid adsorption system. This quantity is typically assessed by directly measuring or calculating (indirectly measuring) the isosteric enthalpy of adsorption: the difference in enthalpy between the adsorbed fluid phase and the bulk fluid phase. This is the quantity chosen since the closed adsorption system is held at constant pressure and temperature, and hence will tend toward minimum Gibbs free energy at equilibrium, wherein the entropic contribution ($T\Delta S_{ads}$) is balanced by the change in enthalpy (ΔH_{ads}). If the difference in molar volume between the two fluids is large (i.e., $\Delta v_{ads} = v_a - v_g \approx v_g$), then the enthalpy of adsorption is simply offset from the binding energy (ΔU_{ads}) by a "constant" factor of Pv_g. Optimizing the isosteric enthalpy of adsorption is an oft-cited goal in efforts to design and synthesize new materials for fluid separation or storage applications.[17-19] In the case of fluid separations, increasing the disparity between the enthalpy of adsorption of the fluids in question

(i.e., improving selectivity) is the fundamental strategy. For facile (reversible) adsorptive fluid storage, the strategy is to achieve a binding strength intermediate between "too strong" and "too weak"; for storage at near ambient conditions, this corresponds to a quantity of ~15-30 kJ mol^{-1}.[20]

Despite that a stated common strategy in materials research is to "optimize" (or sometimes "enhance") the enthalpy of adsorption, it is much less common that the dependence of enthalpy of adsorption on the amount adsorbed (i.e., as adsorption increases) is assessed. This is an important and consequential omission for any adsorption applications (separations or storage) that take place at high pressures where the adsorbed amount is high. A simple Langmuir analysis of a hypothetical adsorptive storage system shows that the dependence of the binding energy on the adsorbed amount (adsorption occupancy) plays a primary role in determining the "deliverable storage quantity" above a minimum system pressure. To maximize the delivered quantity, an "increasing" binding energy (or decreasing negative binding energy) is desired as the surface accumulates more and more adsorbed occupants. If the binding energy is identical under all conditions (as in Langmuir's simplest theory), the delivered amount is often less than if the binding energy is slightly lower but increasing as a function of increased adsorption. A simple demonstration of this effect is shown in Figure 3.

A primary challenge in determining the isosteric enthalpy of adsorption, especially as a function of adsorbed amount, is the reliance of this quantity on the determination of the absolute adsorption quantity, n_a, from the measured "excess

adsorption" quantity, n_e. A model is required for this conversion, and the choice of model affects the calculated result. While this issue is well-known in the adsorption community,[21] it is rarely acknowledged in the characterization of new adsorption systems, especially because there are rarely enough data collected in a single study to genuinely survey the effects of the model on the resulting thermodynamic calculations, and because this type of survey is time-consuming. A crucial feature of any model is the number of independent fitting parameters, N, which should be minimized to avoid "over-fitting" of the data. The single-site Langmuir equation[22] has at minimum a single fitting parameter to describe adsorption site occupancy (a second, the exponential prefactor in an Arrhenius relation, is typically added); two additional parameters are used to then obtain the excess adsorption quantity, leading to $N = 4$. All other physically meaningful adsorption models have the same number of independent fitting parameters or more.

Herein, we investigate the role of the adsorption model, and specifically the conversion of the excess adsorption quantity into the absolute adsorption quantity, on the resulting calculations of isosteric enthalpy of adsorption as a function of surface occupancy. In past work, we reported the success of a dual-site Langmuir equation ($N = 7$) for fitting supercritical methane adsorption on several carbonaceous adsorbents at high pressures.[23, 24] Alternative models include the Tóth equation ($N = 5$),[25] the Unilan equation ($N = 5$),[26] and the Sips equation ($N = 5$),[27, 28] all with fewer independent fitting parameters than the dual-site Langmuir equation. All of these models enjoy the benefit of an analytic solution to

the Clapeyron equation, by which a global description of the isosteric enthalpy of adsorption is accessible. Hence, it is possible to compare the resulting thermodynamic calculations based on each model across the entire range of adsorption amount measured. In performing this comparison, it has become clear that the most important features of the models are: 1) the number of binding sites permitted, and 2) the treatment of the growth of the adsorbed phase, which is subject to typically one of two simple approximations. The results can be compared to those obtained by an "isoexcess" approach which eschews any dependence on the latter approximations, instead relying on one fundamental approximation that the excess adsorbed amount is equal to the absolute adsorbed amount. Finally, the error introduced by neglecting the role of helium adsorption on the carbonaceous adsorbent during volume calibrations is also assessed.

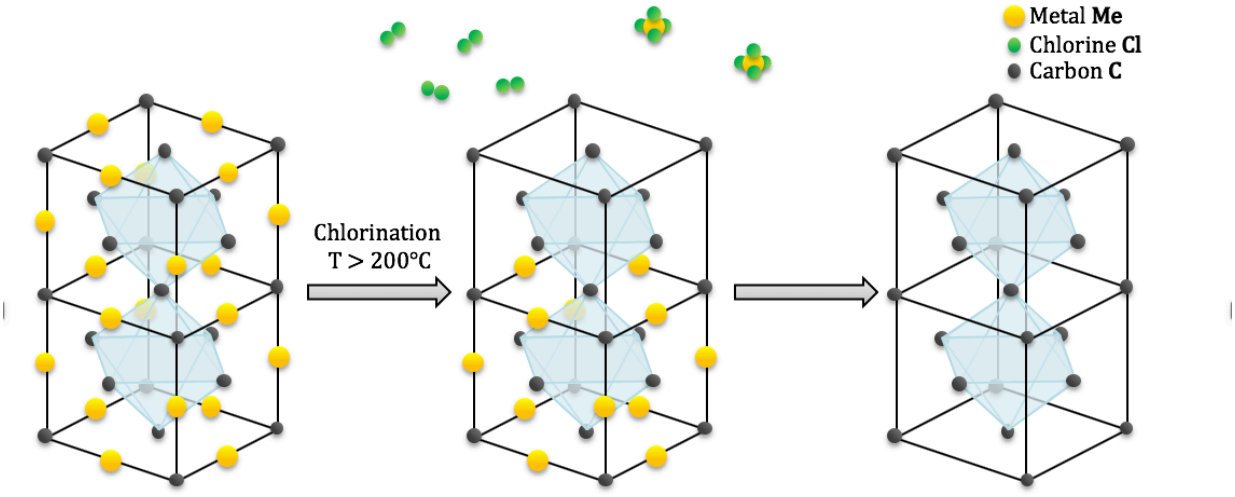

$$MeC_{(s)} + \frac{x}{2}Cl_{2\,(g)} \rightarrow C_{(s)} + MeCl_{x\,(g)}$$

Figure 1. Schematic showing the process as a metal carbide (MeC) transitions to a carbide-derived carbon (CDC) when undergoing the traditional synthesis route via halogenation using chlorine gas at elevated temperatures (>200°C).

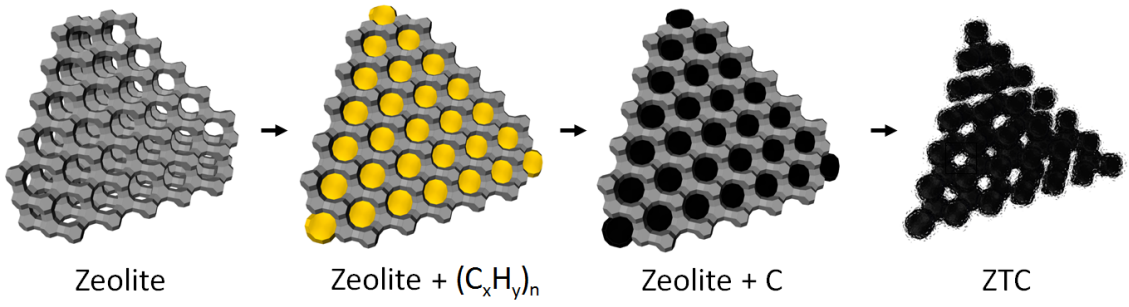

Figure 2. Schematic for the synthesis of a porous zeolite-template being carbonized, resulting in a zeolite-templated carbon (ZTC). Reprinted with permission.[14]

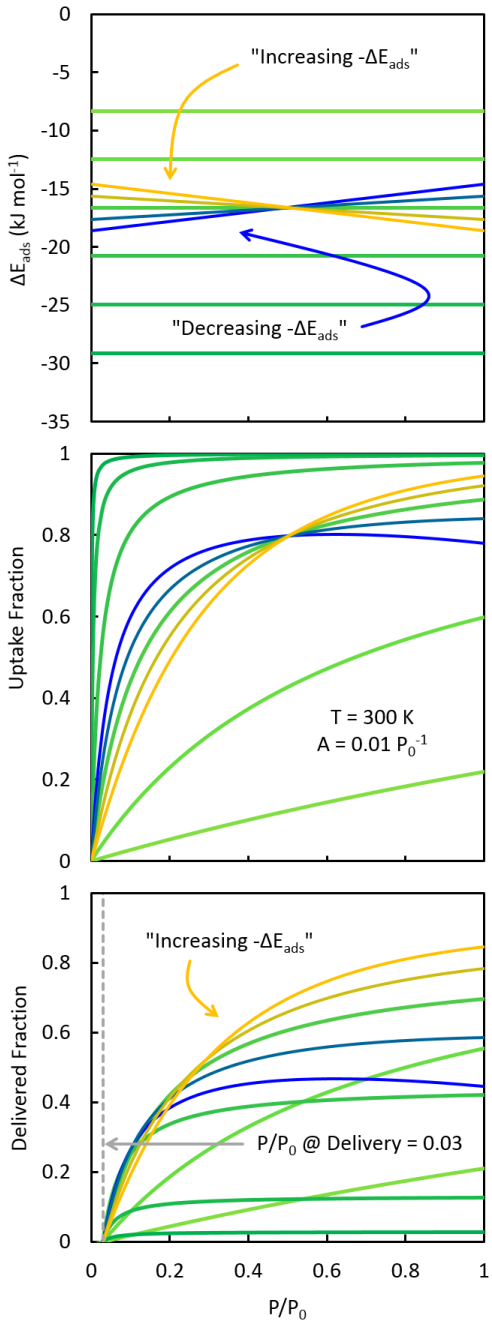

Figure 3. Schematic showing the "delivered fraction" of adsorptive from an adsorption-based storage system characterized by several different distributions of adsorption sites: identical strongly binding sites (dark green), identical "optimized" binding energy sites (medium green), identical weakly binding sites (light green), and distributions of non-identical sites around the "optimized" binding energy (yellow to blue).

CHAPTER TWO

METHODS

2.1 Experimental Methods

A set of equilibrium methane adsorption isotherms was measured on several carbonaceous adsorbent materials between 238-526 K and 0.01-9 MPa, as reported elsewhere.[23] Herein we devote primary focus to the six methane adsorption isotherms on a commercial coconut shell-derived activated carbon, CNS-201 (whose pore structure and materials properties are well-known and have been extensively reported elsewhere[24, 29-32]). CNS-201 has a modest specific surface area of ~1100 $m^2 g^{-1}$ and a pore-size distribution containing exclusively narrow micropores (<1 nm). Two additional materials are used for comparison: MSC-30, a commercially available superactivated carbon (formerly known as AX-21) with a high specific surface area of ~3000 $m^2 g^{-1}$ and a diversity of micropores,[24, 29, 33] and zeolite-templated carbon (ZTC),[34] an ordered porous carbon material with a high specific surface area of ~3600 $m^2 g^{-1}$ and homogeneous micropores of ~1.2 nm in width. Pore-size distributions and surface area analysis of all three materials can be found in previous work.[23]

Due to its commercial availability and specific surface area close to several other readily available carbonaceous adsorbents, CNS-201 serves as the standard material of investigation in this work. This is especially motivated by efforts to account for the (typically neglected) role of helium adsorption at room temperature,

for which there is a similar material for direct comparison: BPL carbon (an activated carbon with a reported BET surface area of ~1125 $m^2\ g^{-1}$).[35] Six equilibrium adsorption isotherms of methane on CNS-201 were collected, comprising 99 individual adsorption equilibrium measurements (where the "raw data" are pressure, temperature, and excess quantity adsorbed). Equilibrium was assessed after waiting for 30 min at each step, and adsorption was completely reversible (showing no desorption hysteresis) under all conditions investigated. Adsorption isotherms were measured between 247-526 K and temperature fluctuations within a given isotherm were $< \pm 0.4$ K at all temperatures investigated. The skeletal density of CNS-201 was measured to be 2.1 g mL^{-1} using standard helium pycnometry methods at room temperature.

2.2 Data Analysis

The raw adsorption data, excess adsorption uptake (n_e^*, in units of mmol g^{-1}) as a function of temperature (T, in units of K) and pressure (P, in units of MPa), were fitted to 15 different models for systematic comparison. The abbreviated nomenclature used to refer to these models is given in Table 1. Fitting the adsorption equilibria was performed using a least-squares residual minimization algorithm based on a differential evolution (stochastic, population-based) method as implemented by a custom Python script (implementing the Coolprop database[36] to determine bulk methane density). The maximum number of iterations over which the entire population was evolved was set to 2000, the

differential evolution strategy was "RandToBest1Bin," and the type of population initialization was random. Each minimization was performed in excess of seven unique times per fit (by varying the random number seed) allowing the exploration within wide limits of each of the fitting parameters (e.g., $0 < n_{max} < 100$ mmol g^{-1}, $0 < V_{max} < 10$ mL g^{-1}, $0 < E_i < 100$ kJ mol^{-1}, and $A_i > 0$). Importantly, each set of data (containing 6-13 isotherms and 99-202 unique equilibrium data points) was fitted globally for a single material. Finally, the isosteric enthalpy of adsorption was calculated using an analytic expression for ΔH_{ads} derived by solving the Clapeyron equation for the given adsorption model.

The goodness of fit of each model was assessed by calculating three statistics: the residual sum of squares per data point ($RSS\ pt^{-1}$), the coefficient of determination (R^2), and the so-called "adjusted" coefficient of determination (R_a^2). The latter figure of merit penalizes models that accrue too many independent parameters,[37] and is the primary criterion for goodness of fit in this work. Over the 99 adsorption equilibria data points measured for CNS-201, these figures of assessment are defined as:

$$\sum_{j=1}^{99}\left(n_{e,j}^{*} - n_{e,j}\right)^2 = RSS \qquad \text{Equation 1}$$

$$\sum_{j=1}^{99}\left(n_{e,j}^{*} - \bar{n}_{e}^{*}\right)^2 = SS_{tot} \qquad \text{Equation 2}$$

$$\frac{1}{99}RSS = RSS\ pt^{-1} \qquad \text{Equation 3}$$

$$1 - \frac{RSS}{SS_{tot}} = R^2 \qquad \text{Equation 4}$$

$$1 - \frac{(99-1)(1-R^2)}{99-N-1} = R_a^2 \qquad \text{Equation 5}$$

In the above equations, $n_{e,j}^*$ refers to a measured excess quantity of adsorption and $n_{e,j}$ refers to the model estimated (fitted) quantity at the same temperature and pressure. The simple average of all measured excess adsorption quantities (at all temperatures and pressures) is referred to as $\bar{n}_e^*$. The above described methodological fitting routine was also applied to the same set of data after being subjected to "correction" based on the error introduced by improper void volume measurement;[35] in the "corrected" case, the measured quantity of excess adsorption is replaced by the corrected quantity. This correction is described in the Helium Adsorption Correction section below.

2.3 Adsorbed Phase Volume Growth

The fundamental relationship between the absolute adsorbed quantity, n_a, and the Gibbs excess (measured) adsorption quantity, n_e, is:

$$n_e = n_a - V_a(P,T)\,\rho_g(P,T) \qquad \text{Equation 6}$$

The bulk fluid density, ρ_g, is an accurately tabulated quantity as a function of temperature and pressure (e.g., in the NIST Refprop database[38]). Ambiguity arises in how to deal with the adsorbed phase volume, $V_a(P,T)$, a function of temperature

and pressure that is difficult or impossible to measure and taken to be well outside the scope of most experimental adsorption studies. A simple model must then be employed to estimate the absolute volume of the adsorbed phase at each equilibrium measurement in order to determine the absolute quantity of adsorption. Two common models are employed, referred to herein as Growth Models 1 and 2 (referring to the "growth" of the adsorbed phase, since it logically increases as adsorption occurs). A third model, referred to herein as Growth Model 3, is also investigated as a compromise between Growth Models 1 and 2, which are defined as follows:

$$\text{Growth Model 1.}\ V_a(T,P) = \theta(T,P)\ V_{max} \qquad \text{Equation 7}$$

$$\text{Growth Model 2.}\ V_a(T,P) = V_{max} = constant \qquad \text{Equation 8}$$

$$\text{Growth Model 3.}\ V_a(T,P) = \theta_{growth}(P)\ V_{max} = \frac{K_{growth}P}{1 + K_{growth}P}\ V_{max} \qquad \text{Equation 9}$$

In Growth Model 1, the volume ascribed to the adsorbed phase increases as adsorption progresses; the increase is held to occur proportionally to the quantity of adsorption, n_a. This implies a constant adsorbate molar volume, v_a, which is determined by setting the total adsorbed phase volume at maximum adsorption occupancy to be an independent parameter of the overall model: V_{max}. In Growth Model 2, the absolute volume ascribed to the adsorbed phase is constant under all conditions, and is set as an independent fitting parameter of the overall model: V_{max}. In this case, the adsorbate molar volume, v_a, is a widely varying quantity, inversely

proportional to the quantity of adsorption, n_a. In Growth Model 3, an intermediate model is imposed, allowing the volume ascribed to the adsorbed phase to increase as adsorption progresses but not requiring it to be directly proportional to the amount adsorbed; rather, the volume grows according to an additional temperature-independent, single-site Langmuir equation growth model. This Langmuir-like growth was arbitrarily chosen for its simplicity and requires a single additional independent parameter, referred to as K_{growth}. The molar volume of the adsorbed phase in each Growth Model is summarized as follows:

$$\text{Growth Model 1. } v_a(T,P) = \frac{\theta(T,P)\,V_{max}}{n_a(T,P)} = \frac{V_{max}}{n_{max}} = constant \qquad \text{Equation 10}$$

$$\text{Growth Model 2. } v_a(T,P) = \frac{V_{max}}{n_a(T,P)} \qquad \text{Equation 11}$$

$$\text{Growth Model 3. } v_a(T,P) = \frac{\theta_{growth}(P)\,V_{max}}{n_a(T,P)} \qquad \text{Equation 12}$$

The same three growth model types were applied to both uncorrected as well as helium-corrected models. A schematic depiction comparing the "physical picture" of adsorption for each of the three Growth Models is shown in Figure 4.

2.4 Adsorption Equilibrium Models

Several well-known adsorption equilibrium models were employed and compared in this work to determine the extent of the model-dependence of the subsequent thermodynamic results. Five simple models were selected using the

following criteria: convergence to Henry's law at low pressure and an analytic solution to the Clapeyron equation (i.e., an analytic expression for the isosteric enthalpy of adsorption). The five models are the single-site Langmuir equation, dual-site Langmuir equation, uniform Langmuir ("Unilan") equation, Tóth equation, and Sips equation.

The single-site Langmuir model is the simplest thermodynamically consistent model of adsorption.[22] It is designed to describe an ideal system where the surface occupancy of the adsorbed gas at a fixed temperature depends only on the gas pressure above the surface of a material and was derived with the following assumptions: the adsorption sites are identical to one another, only a single molecule occupies each site, and the distribution of energy and molecules amongst the sites are independent of the adsorbed quantity. The well-known form of the single-site Langmuir equation is:

$$n_a = n_{max} \frac{KP}{1 + KP} \qquad \text{Equation 13}$$

Likewise, the dual-site Langmuir equation, which assumes that the adsorption sites are divided into two distinct types (each with a unique characteristic binding energy), is given as:

$$n_a = n_{max} \left((1 - \alpha) \left(\frac{K_1 P}{1 + K_1 P} \right) + \alpha \left(\frac{K_2 P}{1 + K_2 P} \right) \right) \qquad \text{Equation 14}$$

In both of the above Langmuir equations of adsorption, we take the Langmuir constant (K or K_i) to have the following simple form:

$$K = A\, e^{-E/RT} \qquad \text{Equation 15}$$

The characteristic binding energies (E or E_i) are held to be an inherent property of the adsorbent and hence independent of temperature and pressure.

The Unilan equation is an extension of Langmuir's simple adsorption model that accounts for a distribution of different adsorption sites.[39] The binding energies of all sites are taken to be unique and uniformly distributed between E_{min} and E_{max}, which is equivalent to a sum over n_{max} different single-site Langmuir equations. The homogeneous distribution of binding energies greatly simplifies the resulting isotherm equation.[40] The Unilan equation has the form:

$$n_a = n_{max}\left(\frac{RT}{E_{min} - E_{max}}\right) ln\left(\frac{a + Pe^{\frac{E_{max}}{RT}}}{a + Pe^{\frac{E_{min}}{RT}}}\right) \qquad \text{Equation 16}$$

where $a = e^{\left(\frac{-\Delta S}{R}\right)}$. By assuming that the adsorption enthalpies between E_{min} and E_{max} are uniformly distributed and zero outside of these bounds, the number of independent fitting parameters is reduced from $N > n_{max}$ (where n_{max} is the number of binding sites) to $N = 5$.

The Tóth adsorption model is an empirical modification of the single-site Langmuir model that is designed to handle heterogenous surfaces.[41] The

parameter t is interpreted as a measure of surface heterogeneity, where $t = 1$ represents a homogenous surface. The Tóth equation has the form:

$$n_a = n_{max} \frac{KP}{(1 + (KP)^t)^{\frac{1}{t}}} \qquad \text{Equation 17}$$

The Tóth binding constant, *K*, is defined herein by an Arrhenius-type equation as in Equation 15 and is equal to the Langmuir binding constant if the surface is homogeneous (i.e., if $t = 1$).[42]

The Sips equation is derived by an empirical combination of the Langmuir and Freundlich models, and much like the Tóth equation, can be used to assess adsorption on heterogeneous surfaces.[27] The Sips equation is given as:

$$n_a = n_{max} \frac{(KP)^{\frac{1}{m}}}{1 + (KP)^{\frac{1}{m}}} \qquad \text{Equation 18}$$

The Sips binding constant, K, is defined herein by an Arrhenius-type equation as in Equation 15 and is equal to the Langmuir binding constant if the surface is homogeneous (i.e., if $m = 1$).

2.5 Isosteric Heat of Adsorption

The thermodynamic quantity of interest for adsorbent materials is the isosteric enthalpy of adsorption, ΔH_{ads}, a difference that is negative under most conditions but is often reported as a positive value, q_{st}, and referred to as the

isosteric heat of adsorption. The general form of the Clapeyron equation used to determine the isosteric enthalpy of adsorption is:

$$\Delta H_{ads} = H_a - H_g = T\left(v_a - \frac{1}{\rho_g}\right)\left(\frac{\partial P}{\partial T}\right)_{n_a} \qquad \text{Equation 19}$$

For each model there exists an analytic solution to the above equation that gives the isosteric enthalpy of adsorption as a function of the independent fitting parameters, temperature, and pressure. For example, for a single-site Langmuir model combined with Growth Model 1 (SL1), the isosteric enthalpy of adsorption is:

$$\Delta H_{ads} = T\left(v_a - \frac{1}{\rho_g}\right)\left(\frac{EP}{RT^2}\right) = \left(\frac{V_{max}}{n_{max}} - \frac{1}{\rho_g}\right)\frac{PE}{RT} \qquad \text{Equation 20}$$

This expression abstains from two common approximations (that the bulk fluid is an ideal gas, and that the molar volume of the adsorbed phase is negligible compared to that of the bulk fluid), making it applicable to adsorption under high pressure conditions. It should be noted that Equation 20 reduces to a very simple expression ($\Delta H_{ads} = -E$) when the above approximations are employed. The corresponding equations for the enthalpy of adsorption for the remaining fourteen models explored in this work are given in the Supporting Information.

2.6 Helium Adsorption Correction

Helium adsorption at room temperature during void volume determinations (i.e., measurements of skeletal density) accounts for a slight error in the subsequent

measurements of adsorption equilibria of the species of interest (e.g., methane). The extent of this error is not fully understood, but has been estimated in previous reports to be significant.[35] Since helium adsorption is so weak at near ambient temperatures, its adsorption isotherm is well-approximated by Henry's Law; therefore, only the magnitude of the Henry's Law constant is needed to correct for the role of helium in overestimation of the void volume (and subsequent underestimation of the adsorbed quantity of the adsorbate of interest). It has been suggested to employ the following correction:

$$n_{e,corr} = n_e^* + K_{He}\,\rho_g \qquad \text{Equation 21}$$

In this expression, the gas density refers to the adsorbate of interest in the adsorption experiments (in this work, methane). The correction factor must be determined experimentally for a given material, requiring accurate measurements of the quantity of helium adsorbed on the sample at room temperature. Previously reported values for porous carbon materials were found to be proportional to BET surface area, and hence it is possible to estimate the correction factor for materials of similar surface area to those previously investigated.[35, 43] For CNS-201, of approximately the same surface area and helium binding energy as BPL carbon, the following correction factor is used: $K_{He} = 0.2791593$.

2.7 Isoexcess Heat of Adsorption

The isosteric method is known to have several shortcomings that make unambiguous determination of the true enthalpy of adsorption a challenge.[44, 45] The primary issues are that estimation of the absolute quantity of adsorption is required, which is both model dependent (in terms of the overall adsorption equation employed) and requires an approximation of the adsorbed phase density (which is the topic of this work).[46] It has been suggested that the as-measured excess adsorption equilibria could simply be used to approximate the absolute adsorption equilibria without the use of a model (i.e., treating $n_e \approx n_a$ and performing interpolation only), referred to as the "isoexcess" method.[44] However, the resulting "isoexcess" enthalpies of adsorption often do not show physically reasonable behaviors (including a sharp rise at high adsorption amounts) owing to the prevalence of the excess adsorption maximum, especially at low temperatures and high pressures.[47] The merits of the isoexcess method versus those of the isosteric method remain under active discussion.[48]

For comparison to the isosteric method employed in this work, a fitting and thermodynamic analysis method referred to as the "isoexcess" method has also been applied. In this method, each set of isotherms (the raw data) is globally fitted to one of five equations (the same as in Equation 13-18 except without any consideration of the volume of the adsorbed phase since the measured excess quantity is taken to be the absolute quantity of adsorption). For example, for a single-site Langmuir model (ISL), the experimental data are fitted directly as:

$$n_e = n_{max} \frac{KP}{1 + KP} \qquad \text{Equation 22}$$

It should be noted that each adsorption equation employed in this isoexcess method has one less independent fitting parameter than the equivalent equation employed in the isosteric method. The isoexcess enthalpy of adsorption is then found by a modified form of the Clapeyron equation that also ignores the volume of the adsorbed phase (i.e., $v_a = 0$):

$$\Delta H_{ads,iso} = T\left(-\frac{1}{\rho_g}\right)\left(\frac{\partial P}{\partial T}\right)_{n_e} \qquad \text{Equation 23}$$

In this work, the molar volume of the bulk fluid is still taken to be that of real methane (not an ideal gas) and the pressure is preserved in all equations and calculations (as opposed to other methods which convert from the pressure to fugacity and then utilize the Clausius-Clapeyron equation directly). While the isoexcess approach employed herein is inherently model dependent, it is not dependent on any approximation of the growth of the volume of the adsorbed phase.

The modeless approach was also employed in this work. This method treats $n_e \approx n_a$ and remains model independent by interpolating the raw data rather than globally fitting the data to the five different adsorption models. Therefore, no fit parameters are required and an approximation for the absolute adsorption equilibria can be obtained. Equation 23 still holds for this approach, however, the

average temperature and density of the gas phase were used instead of local values. Furthermore, two isotherms were used to calculate the partial differential of pressure with respect to temperature.

Table 1. Adsorption model nomenclature.

		Growth Model 1 (constant ρ_a) $V_a = \theta\ V_{max}$	Growth Model 2 (constant V_a) $V_a = V_{max}$	Growth Model 3 (empirical V_a) $V_a = \theta_{SL}\ V_{max}$
Uncorrected	Langmuir	SL1	SL2	SL3
	Dual-Site Langmuir	DL1	DL2	DL3
	Unilan	UL1	UL2	UL3
	Tóth	TO1	TO2	TO3
	Sips	SP1	SP2	SP3
Helium-Corrected	Langmuir	HSL1	HSL2	HSL3
	Dual-Site Langmuir	HDL1	HDL2	HDL3
	Unilan	HUL1	HUL2	HUL3
	Tóth	HTO1	HTO2	HTO3
	Sips	HSP1	HSP2	HSP3
		Isoexcess Model Uncorrected $V_a = 0$	Isoexcess Model Helium-Corrected $V_a = 0$	
Isoexcess	Langmuir	ISL	HISL	
	Dual-Site Langmuir	IDL	HIDL	
	Unilan	IUL	HIUL	
	Tóth	ITO	HITO	
	Sips	ISP	HISP	

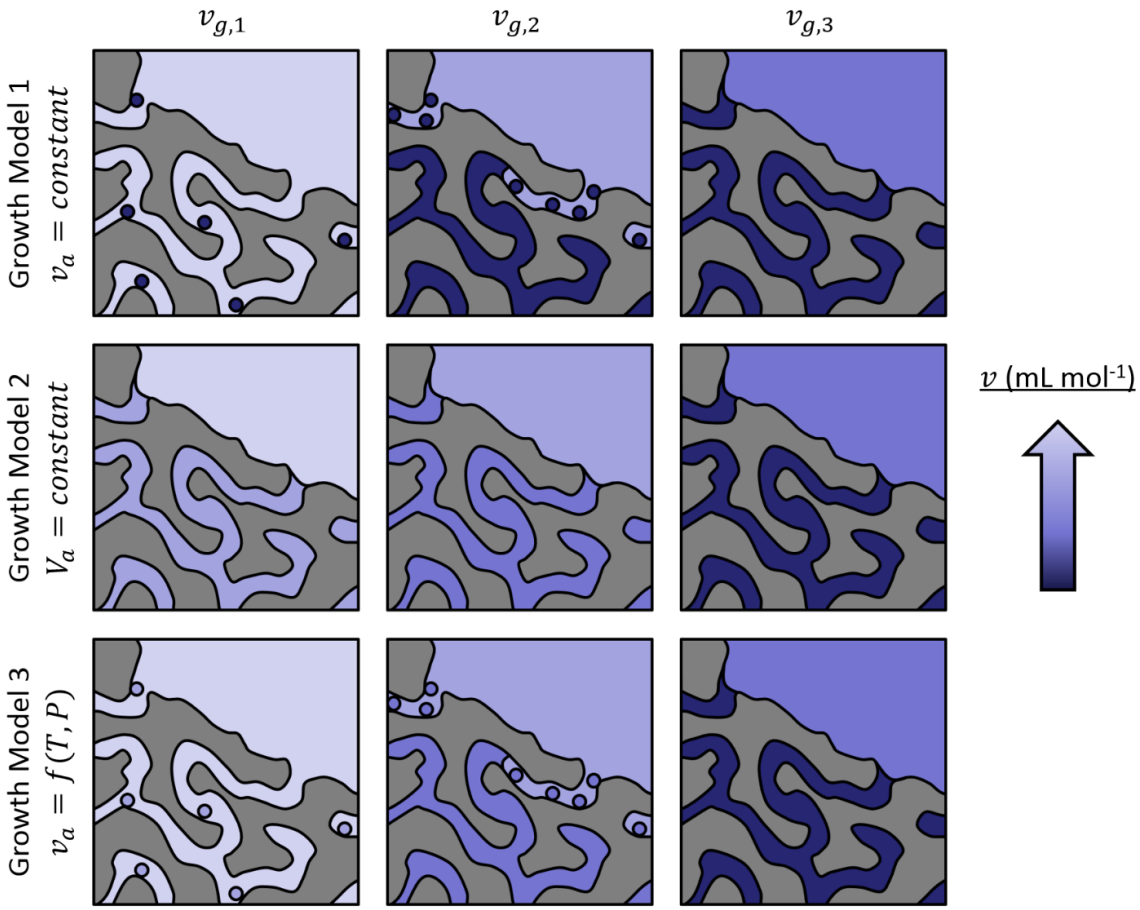

Figure 4. Schematic depiction of three adsorbed phase volume growth models employed in this work: Growth Model 1 (constant adsorbed phase density), Growth Model 2 (constant adsorbed phase volume), and Growth Model 3 (variable adsorbed phase density and volume). Adsorbate fluid is shown in purple (shaded to indicate increasing density, or decreasing molar volume) and solid adsorbent is shown in gray.

CHAPTER THREE

RESULTS

3.1 Goodness of Fit Criteria

Fifteen different methodologies for globally fitting and extracting thermodynamic properties from measured excess adsorption equilibria were applied for comparison and interpretation of the role of the model in the resulting thermodynamic calculations. The number of independent parameters in each case, N, varies from 4 (e.g., SL1 and SL2) up to 8 (e.g., DL3). The goodness of fit of each model is assessed by comparing either of two statistics: the residual sum of squares per data point (RSS pt^{-1}) and the so-called "adjusted" coefficient of determination (R_a^2). The latter figure of merit penalizes models that accrue unnecessarily many independent parameters,[37] and is the primary criterion for goodness of fit in this work. In addition to a purely statistical justification of the fitness of a model, the ultimate density of the adsorbed phase upon maximum adsorption site occupancy, $\rho_{a,max}$, is also assessed for physical reasonability. This value should be similar in magnitude to that of liquid methane at the normal boiling point: 26.3 mol L^{-1}.[49] The best fit parameter values and figures of assessment are shown in Table 2 and Table 3.

3.2 Fitting of Uncorrected Methane Adsorption on CNS-201

The best fits of the raw (uncorrected for helium adsorption) adsorption equilibria to each of the fifteen models are shown in Figure 5 and the corresponding best fit parameters are shown in Table 2. The single-site Langmuir models (SL1, SL2, and SL3) were the least successful at fitting supercritical methane adsorption on CNS-201 between 247-526 K, exhibiting the highest RSS pt^{-1} and lowest R_a^2 values of the models explored herein. The fits are especially poor at low temperatures where an excess maximum is observed in the measured data. The adsorbed phase densities for SL1 and SL2 are >2× higher than that of normal liquid methane, an indication of unphysical fitment of the maximum volume available to the adsorbed phase relative to the total number of adsorption sites.

The dual-site Langmuir models (DL1, DL2, and DL3) and the Tóth models (TO1, TO2, and TO3) were the most successful at fitting supercritical methane adsorption on CNS-201 between 247-526 K, exhibiting the lowest RSS pt^{-1} and highest R_a^2 values of the models explored herein. In both cases, Growth Model 1 demonstrates the highest statistical goodness of fit, as determined by the adjusted coefficient of determination (R_a^2); DL1 is the overall best fit, as originally reported,[23] even when considering the additional independent fitting parameters employed. The maximum density of the adsorbed phase for both DL1 and TO1 is ~80% that of normal liquid methane, while DL2, DL3, TO2, and TO3 predict a maximum adsorbed phase density that is 15-30% higher. The Sips models (SP1, SP2, and SP3) are statistically less accurate, and the Unilan models (UL1, UL2, and

UL3) are ranked fourth overall. Growth Model 3, a compromise between Growth Models 1 and 2, could not be well justified for any fit based on an analysis of the adjusted coefficient of determination; instead, Growth Model 3 fits tended to "snap" into a similar local minimum of squared residuals as those of Growth Model 2 fits which benefit from one less arbitrary complexity.

There are several notable trends in the best fit parameters that persist across all models employed. The three most statistically favored fitting model types (the DL, TO, and SP series) yielded similar values for the maximum number of adsorption sites ($n_{max} = 9.4 - 11.0$ mmol g^{-1}) and maximum volume of the adsorbed phase ($V_{max} = 0.35 - 0.52$ mL g^{-1}). The former parameter implies an average binding site area (based on the BET surface area as measured by N_2 at 77 K) of 0.18-0.20 nm^2, which is similar to the conventional cross-sectional area of a nitrogen molecule (0.162 nm^2).[50] Likewise, the latter parameter is very similar in magnitude to the total pore volume (based on a single-point analysis as measured by N_2 at 77 K): 0.47 mL g^{-1}. Growth Model 1, across all three statistically favored fitting model types, tended toward higher values for the maximum number of adsorption sites and maximum volume of the adsorbed phase, and likewise tended toward higher values for the binding energy.

3.3 Fitting of Helium Adsorption Corrected Methane Adsorption on CNS-201

When the general "correction" for the role of helium adsorption in the measurement of adsorbent skeletal density (Equation 21) is applied to the raw

excess adsorption isotherms, the primary effect is an increase in the measured quantity adsorbed, and a diminishing or vanishing of the excess adsorption maximum within the conditions investigated (247-526 K and 0-9 MPa). The corrected adsorption equilibria and subsequent best fits to the same fifteen models as applied above are shown in Figure 6. Statistically, the fits follow the same trends observed for the fits of the uncorrected adsorption equilibria: the best fits correspond to the DL and TO models, followed by the SP models, then the UL models, and finally the SL models (see Table 3). Due to the absence of an adsorption maximum within the range measured, the SL models fit best without any volume ascribed to the adsorbed phase (in other words, directly validating an isoexcess approach as described below). An important difference with respect to the DL, UL, TO, and SP fitting results lies in the predicted maximum adsorbed phase density; at maximum coverage, the adsorbed phase is predicted to be significantly denser than that in the uncorrected case, 1.3-5.2× higher than the density of normal liquid methane. Hence, for the purposes of this work, no further thermodynamic analysis of these fits were carried out.

3.4 Isosteric Heat of Adsorption of Methane on CNS-201

The isosteric enthalpy of adsorption of methane on CNS-201 (uncorrected for helium adsorption) at 247, 298, and 526 K, across fifteen different models, is shown in Figure 7. A dependence of $-\Delta H_{ads}$, referred to herein as the isosteric heat of adsorption, on temperature and adsorbed amount, as well as on the global model

used to interpolate the measured data, is observed. All heats of adsorption are found to be monotonically decreasing as a function of adsorption uptake, regardless of temperature or model employed, as expected for a heterogeneous adsorbent surface. The isosteric heat in the Henry's law limit at 298 K, over all models employed, is ~18.3 kJ mol^{-1} within a spread of $\pm$2 kJ mol^{-1}, representing a 10.9% disagreement. This disagreement is consistent across all temperatures between 247-526 K, increasing slightly at higher temperatures (as in Figure 7f).

The isosteric heats of adsorption calculated by the fifteen different methods employed herein fall into three predominant regimes: a "high heat regime" (dark gray in Figure 7) occupied by the SL1, DL1, TO1, and SP1 models, a "low heat regime" (light gray in Figure 7) occupied by the SL2, SL3, DL2, DL3, TO2, TO3, SP2, and SP3 models, and a wide-ranging regime occupied by the UL1, UL2, and UL3 models only (green lines in Figure 7). At 298 K, for example, the high heat regime is 7-8% higher than the low heat regime, but exhibits a similar dependence on adsorbed amount (Figure 7d). The heat of adsorption in both regimes is relatively constant between $n_a = 0 - 4$ mmol g^{-1}, and then declines rapidly as the surface coverage approaches completion. A similar trend is observed in these regimes at 247 K (Figure 7b) and 526 K (Figure 7f), except that the range of surface occupancy explored at the latter temperature is far lower within the measurements performed herein and the decline is not observed. The high heat and low heat regimes represent agreement between four out of the five model types explored herein to within $\pm$1.1 kJ mol^{-1} at 298 K. The third regime is significantly different; the Unilan

models consistently estimate a wider overall range of adsorption enthalpies and a more gradually decreasing heat of adsorption than any of the other models. The agreement along the entire range of absolute quantity adsorbed for UL1 with respect to the high heat regime is $\pm$1.6 kJ mol^{-1}. We also note that at high temperatures, the SL models diverge from the other models in both the high heat and low heat regimes, a result of poor fitting of the measured data.

3.5 Isosteric Heat of Adsorption of Methane on MSC-30 and ZTC

The isosteric enthalpy of adsorption of methane on two additional microporous carbon materials, MSC-30 and ZTC, at 298 K are shown in Figure 8. The heat of adsorption is determined to be significantly smaller (11-16 kJ mol^{-1} in the Henry's Law limit) across all models employed, as consistent with earlier results,[23, 24] owing to the larger pore size(s) in these materials. In addition, the spread between the high heat regime and the low heat regime (corresponding to Growth Model 1 and Growth Models 2 and 3, respectively) is larger for both materials: ~25% higher in the high heat regime for ZTC. The Unilan models, while still representing an outlying third regime, are more consistent with the spread in the results between the high and low heat regimes than in the case for CNS-201.

3.6 Isoexcess Heat of Adsorption of Methane on CNS-201

The best fit parameter values and figures of assessment of methane on CNS-201 as estimated by the isoexcess method are shown in Table 4, for both

uncorrected and helium adsorption corrected results. The enthalpy of adsorption is shown in Figure 9. The five models employed in each case do not distinguish between excess and absolute adsorbed amount since this method accepts the approximation that $n_e \approx n_a$. In principle, no model needs to be employed to interpolate the data and determine the isoexcess heat of adsorption; hence, the result of linear interpolation of the data is also shown. The agreement of the results across all models (including without any model employed) is weak, for the fits and calculations on both uncorrected (Figure 9b) and corrected (Figure 9d) adsorption equilibria. The heat of adsorption of methane on CNS-201 in the Henry's law limit at 298 K is estimated to lie in the range between 13-21 kJ mol^{-1}, a significantly larger range than for the heats estimated by the isosteric method (Figure 7d). As in the isosteric method above, the Unilan model estimates a wider overall range of adsorption enthalpies and a more gradually decreasing heat of adsorption than any of the other models. In the isoexcess method, the Sips model estimates a significantly lower heat of adsorption than the other models.

Table 2. Best fit parameters and figures of assessment for adsorption of methane on CNS-201 between 247-526 K and 0.01-9 MPa based on the raw experimental data.

		Growth 1 (constant ρ_a) $V_a = \theta\ V_{max}$	Growth 2 (constant V_a) $V_a = V_{max}$	Growth 3 (empirical V_a) $V_a = \theta_{SL}\ V_{max}$	Units
Langmuir (SL)	n_{max}	7.315	7.385	7.391	mmol g^{-1}
	V_{max}	0.120	0.130	0.132	mL g^{-1}
	A	0.00097	0.00113	0.00114	MPa^{-1}
	E	17.955	17.554	17.535	kJ mol^{-1}
	K_{growth}	-	-	22.586	MPa^{-1}
	$\rho_{a,max}$	62.152	56.755	55.827	mmol g^{-1} pt^{-1}
	RSS pt^{-1}	0.075	0.074	0.073	unitless
	R_a^2	0.984	0.970	0.984	mol L^{-1}
Dual-Site Langmuir (DL)	n_{max}	9.819	9.50	9.498	mmol g^{-1}
	V_{max}	0.490	0.410	0.410	mL g^{-1}
	α	0.579	0.396	0.604	unitless
	A_1	0.00182	0.0004	0.00302	MPa^{-1}
	E_1	18.755	17.840	17.838	kJ mol^{-1}
	A_2	0.0002	0.0030	0.0004	MPa^{-1}
	E_2	17.407	16.158	16.153	kJ mol^{-1}
	K_{growth}	-	-	100.0	MPa^{-1}
	$\rho_{a,max}$	19.888	22.929	22.918	mmol g^{-1} pt^{-1}
	RSS pt^{-1}	0.004	0.005	0.005	unitless
	R_a^2	0.999	0.999	0.999	mol L^{-1}
Unilan (UL)	n_{max}	13.263	17.225	16.935	mmol g^{-1}
	V_{max}	0.754	0.595	0.60	mL g^{-1}
	ΔS	-9.601	-8.930	-8.981	R
	E_{min}	5.700	0.0	0.0	kJ mol^{-1}
	E_{max}	23.446	21.670	21.820	kJ mol^{-1}
	K_{growth}	-	-	0.153	MPa^{-1}
	$\rho_{a,max}$	17.594	28.926	28.252	mmol g^{-1} pt^{-1}
	RSS pt^{-1}	0.015	0.013	0.012	unitless
	R_a^2	0.997	0.997	0.997	mol L^{-1}

* - "RSS pt^{-1}" refers to the residual sum of squares, per fitted point

** - molar, volume, and pressure quantities in this table refer to CH_4, and per gram quantities refer to the mass of adsorbent (CNS-201)

		Growth 1 (constant ρ_a) $V_a = \theta\ V_{max}$	Growth 2 (constant V_a) $V_a = V_{max}$	Growth 3 (empirical V_a) $V_a = \theta_{SL}\ V_{max}$	Units
Tóth (TO)	n_{max}	10.978	10.377	10.376	mmol g^{-1}
	V_{max}	0.520	0.380	0.380	mL g^{-1}
	A	0.00156	0.00227	0.00227	MPa^{-1}
	E	18.414	17.252	17.251	kJ mol^{-1}
	t	0.490	0.541	0.541	unitless
	K_{growth}	-	-	300.0	MPa^{-1}
	$\rho_{a,max}$	21.165	27.176	27.172	mmol g^{-1} pt^{-1}
	RSS pt^{-1}	0.005	0.006	0.006	mmol g^{-1} pt^{-1}
	R_a^2	0.999	0.999	0.999	mol L^{-1}
Sips (SP)	n_{max}	9.603	9.430	9.430	mmol g^{-1}
	V_{max}	0.412	0.347	0.348	mL g^{-1}
	A	0.000439	0.000538	0.000537	MPa^{-1}
	E	12.679	12.388	12.394	kJ mol^{-1}
	m	1.466	1.410	1.410	unitless
	K_{growth}	-	-	379.747	MPa^{-1}
	$\rho_{a,max}$	23.307	27.138	27.080	mmol g^{-1} pt^{-1}
	RSS pt^{-1}	0.008	0.009	0.009	mmol g^{-1} pt^{-1}
	R_a^2	0.998	0.997	0.998	mol L^{-1}

* - "RSS pt^{-1}" refers to the residual sum of squares, per fitted point
** - molar, volume, and pressure quantities in this table refer to CH_4, and per gram quantities refer to the mass of adsorbent (CNS-201)

Table 3. Best fit parameters and figures of assessment for adsorption of methane on CNS-201 between 247-526 K and 0.01-9 MPa after helium adsorption correction.

		Growth 1 (constant ρ_a) $V_a = \theta\ V_{max}$	Growth 2 (constant V_a) $V_a = V_{max}$	Growth 3 (empirical V_a) $V_a = \theta_{SL}\ V_{max}$	Units
Langmuir (HSL)	n_{max}	7.971	7.971	7.971	mmol g^{-1}
	V_{max}	0.0	0.0	0.0	mL g^{-1}
	A	0.00145	0.00145	0.00145	MPa^{-1}
	E	16.585	16.585	16.585	kJ mol^{-1}
	K_{growth}	-	-	65.298	mmol g^{-1} pt^{-1}
	$\rho_{a,max}$	inf	inf	inf	mmol g^{-1} pt^{-1}
	RSS pt^{-1}	0.083	0.083	0.083	MPa^{-1}
	R_a^2	0.986	0.986	0.986	mol L^{-1}
Dual-Site Langmuir (HDL)	n_{max}	9.670	9.500	9.045	mmol g^{-1}
	V_{max}	0.175	0.135	0.136	mL g^{-1}
	α	0.596	0.604	0.396	unitless
	A_1	0.00254	0.00304	0.00301	MPa^{-1}
	E_1	18.144	17.832	17.853	kJ mol^{-1}
	A_2	0.000313	0.000404	0.000402	MPa^{-1}
	E_2	16.403	16.123	16.128	kJ mol^{-1}
	K_{growth}	-	-	33.416	mmol g^{-1} pt^{-1}
	$\rho_{a,max}$	55.294	70.144	69.788	mmol g^{-1} pt^{-1}
	RSS pt^{-1}	0.004	0.005	0.005	MPa^{-1}
	R_a^2	0.999	0.999	0.989	mol L^{-1}
Unilan (HUL)	n_{max}	13.863	17.226	17.047	mmol g^{-1}
	V_{max}	0.403	0.317	0.323	mL g^{-1}
	ΔS	-9.248	-8.928	-8.952	R
	E_{min}	4.534	0.0	0.0	kJ mol^{-1}
	E_{max}	22.514	21.664	21.734	kJ mol^{-1}
	K_{growth}	-	-	0.120	mmol g^{-1} pt^{-1}
	$\rho_{a,max}$	34.368	54.388	52.737	mmol g^{-1} pt^{-1}
	RSS pt^{-1}	0.013	0.013	0.013	MPa^{-1}
	R_a^2	0.998	0.998	0.998	mol L^{-1}

* - "RSS pt^{-1}" refers to the residual sum of squares, per fitted point

** - molar, volume, and pressure quantities in this table refer to CH_4, and per gram quantities refer to the mass of adsorbent (CNS-201)

		Growth 1 (constant ρ_a) $V_a = \theta\ V_{max}$	Growth 2 (constant V_a) $V_a = V_{max}$	Growth 3 (empirical V_a) $V_a = \theta_{SL}\ V_{max}$	Units
Tóth (HTO)	n_{max}	10.676	10.376	10.385	mmol g^{-1}
	V_{max}	0.153	0.103	0.104	mL g^{-1}
	A	0.00210	0.00227	0.00227	MPa^{-1}
	E	17.504	17.252	17.253	kJ mol^{-1}
	t	0.522	0.541	0.541	unitless
	K_{growth}	-	-	111.895	mmol g^{-1} pt^{-1}
	$\rho_{a,max}$	69.569	101.106	100.279	mmol g^{-1} pt^{-1}
	RSS pt^{-1}	0.006	0.006	0.006	MPa^{-1}
	R_a^2	0.999	0.999	0.999	mol L^{-1}
Sips (HSP)	n_{max}	9.528	9.430	9.437	mmol g^{-1}
	V_{max}	0.0913	0.069	0.0697	mL g^{-1}
	A	0.00523	0.00537	0.00538	MPa^{-1}
	E	12.389	12.394	12.383	kJ mol^{-1}
	m	1.425	1.410	1.410	unitless
	K_{growth}	-	-	292.040	mmol g^{-1} pt^{-1}
	$\rho_{a,max}$	104.336	136.753	135.343	mmol g^{-1} pt^{-1}
	RSS pt^{-1}	0.009	0.009	0.009	MPa^{-1}
	R_a^2	0.999	0.998	0.998	mol L^{-1}

* - "RSS pt^{-1}" refers to the residual sum of squares, per fitted point
** - molar, volume, and pressure quantities in this table refer to CH_4, and per gram quantities refer to the mass of adsorbent (CNS-201)

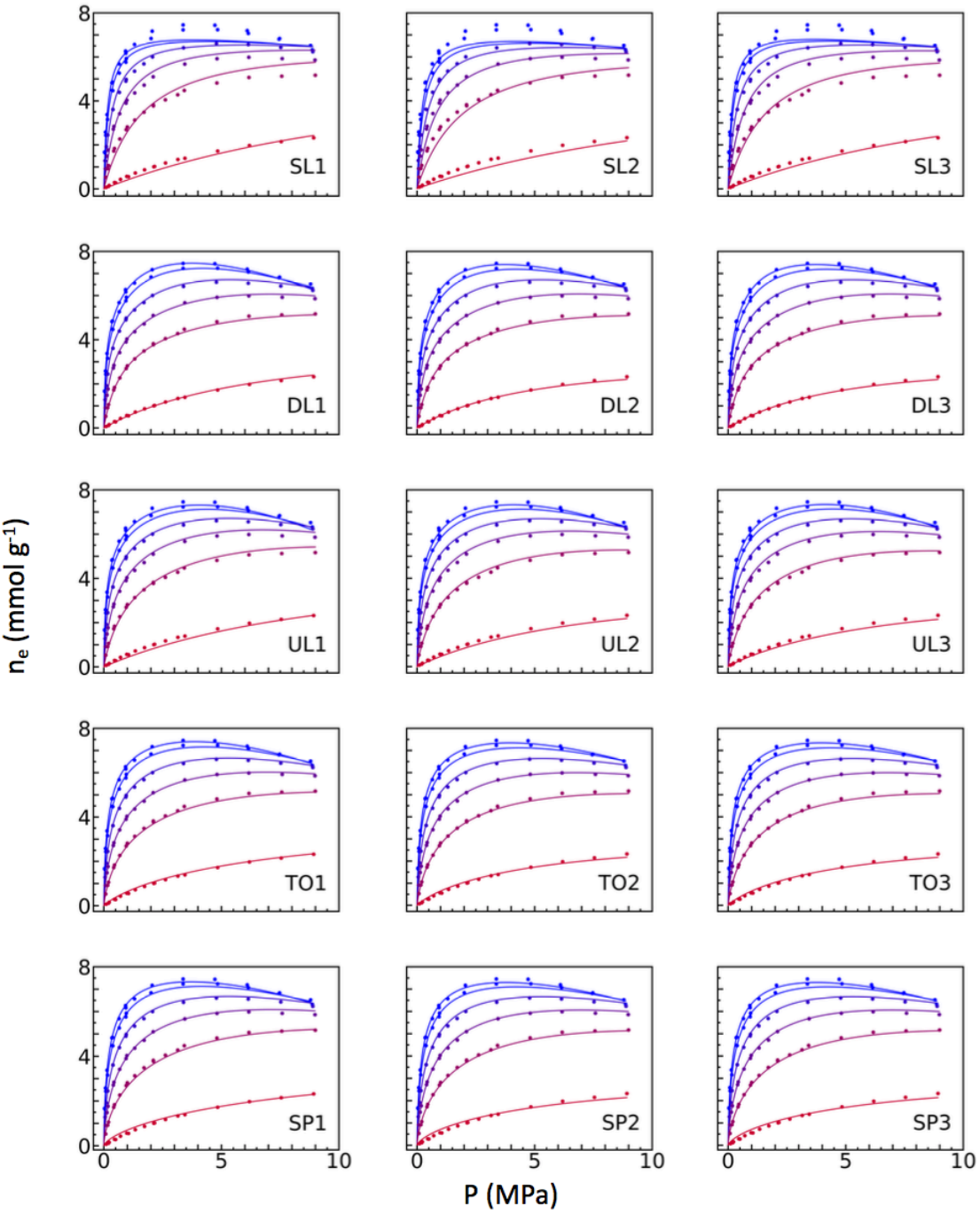

Figure 5. Global best fit results of uncorrected excess adsorption equilibria of methane on CNS-201 by 15 different models. The abbreviated name of each model are shown. The isotherm temperatures are indicated by color, from blue to red: 247, 255, 273, 298, 340 and 526 K, respectively.

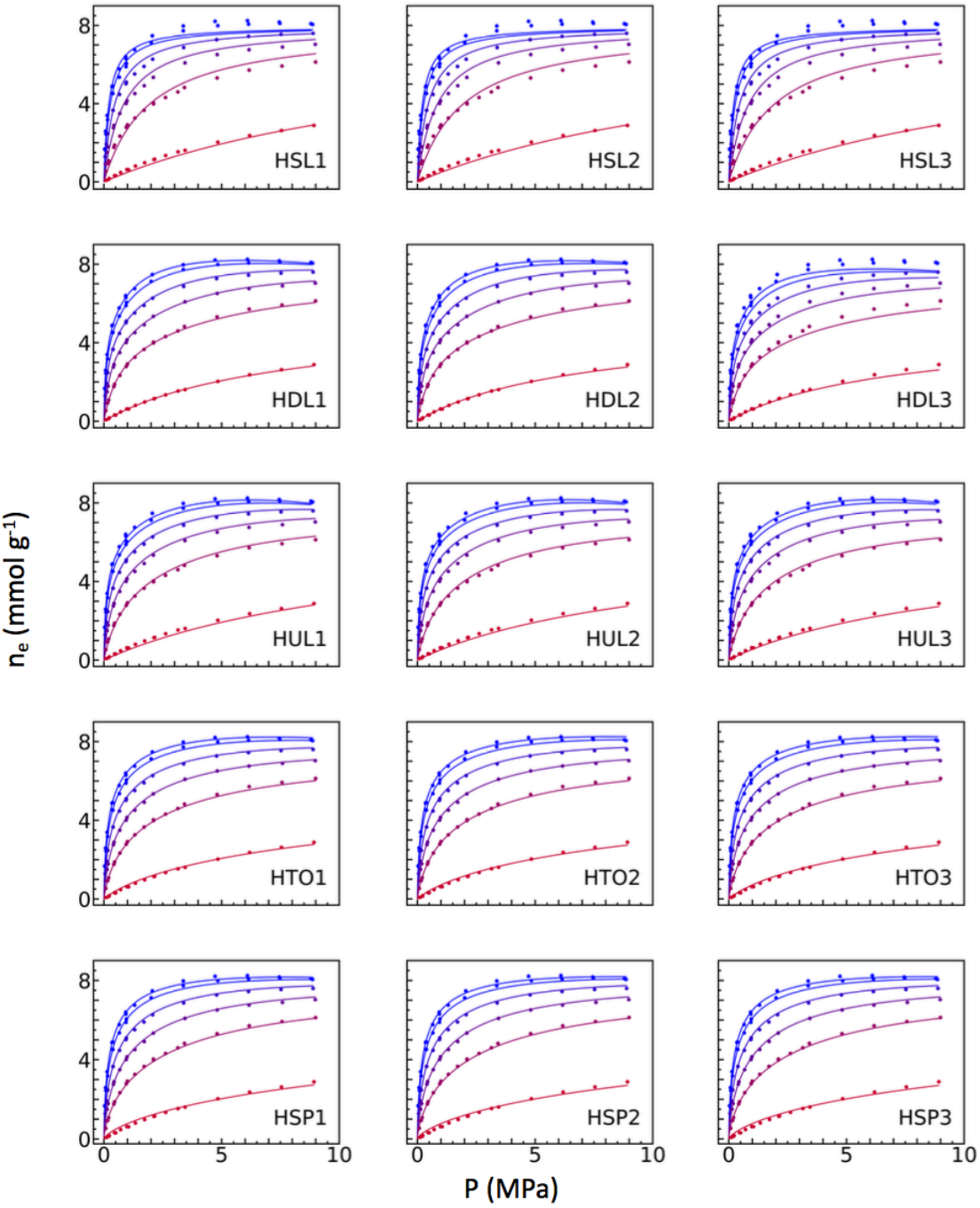

Figure 6. Global best fit results of helium corrected excess adsorption equilibria of methane on CNS-201 by 15 different models. The abbreviated name of each model are shown. The isotherm temperatures are indicated by color, from blue to red: 247, 255, 273, 298, 340 and 526 K, respectively.

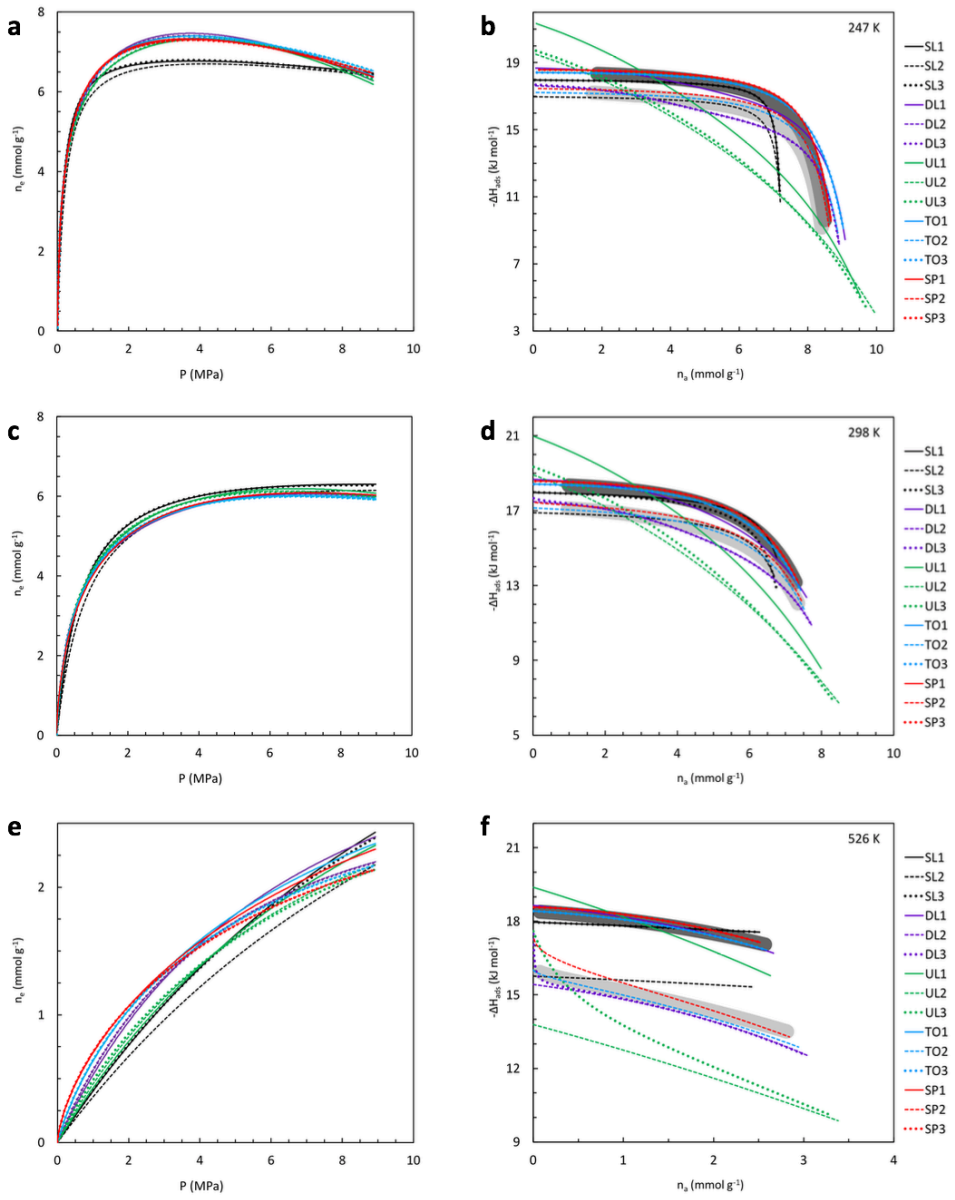

Figure 7. (a) Fitted excess adsorption uptake of methane on CNS-201 between 0.01-9 MPa at 250 K. (b) Isosteric heat of adsorption of methane on CNS-201 as a function of absolute adsorption between 0.01-9 MPa at 250 K, calculated by fifteen different models. (c) Fitted excess adsorption uptake of methane on CNS-201 between 0.01-9 MPa at 298 K. (d) Isosteric heat of adsorption of methane on CNS-201 as a function of absolute adsorption between 0.01-9 MPa at 298 K, calculated by fifteen different models. (e) Fitted excess adsorption uptake of methane on CNS-201 between 0.01-9 MPa at 500 K. (f) Isosteric heat of adsorption of methane on CNS-201 as a function of absolute adsorption between 0.01-9 MPa at 500 K, calculated by fifteen different models.

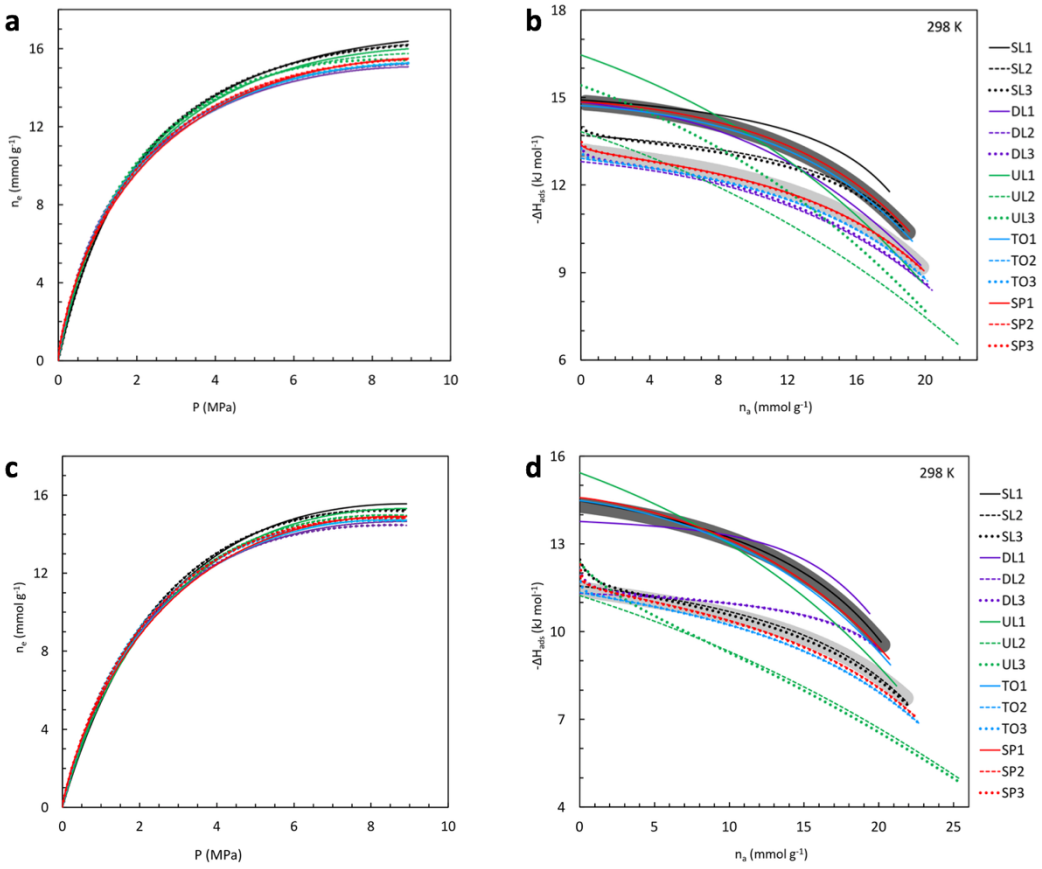

Figure 8. (a) Fitted excess adsorption uptake of methane on MSC-30 between 0.01-9 MPa at 298 K. (b) Isosteric heat of adsorption of methane on MSC-30 as a function of absolute adsorption between 0.01-9 MPa at 298 K, calculated by fifteen different models. (c) Fitted excess adsorption uptake of methane on ZTC between 0.01-9 MPa at 298 K. (d) Isosteric heat of adsorption of methane on ZTC as a function of absolute adsorption between 0.01-9 MPa at 298 K, calculated by fifteen different models.

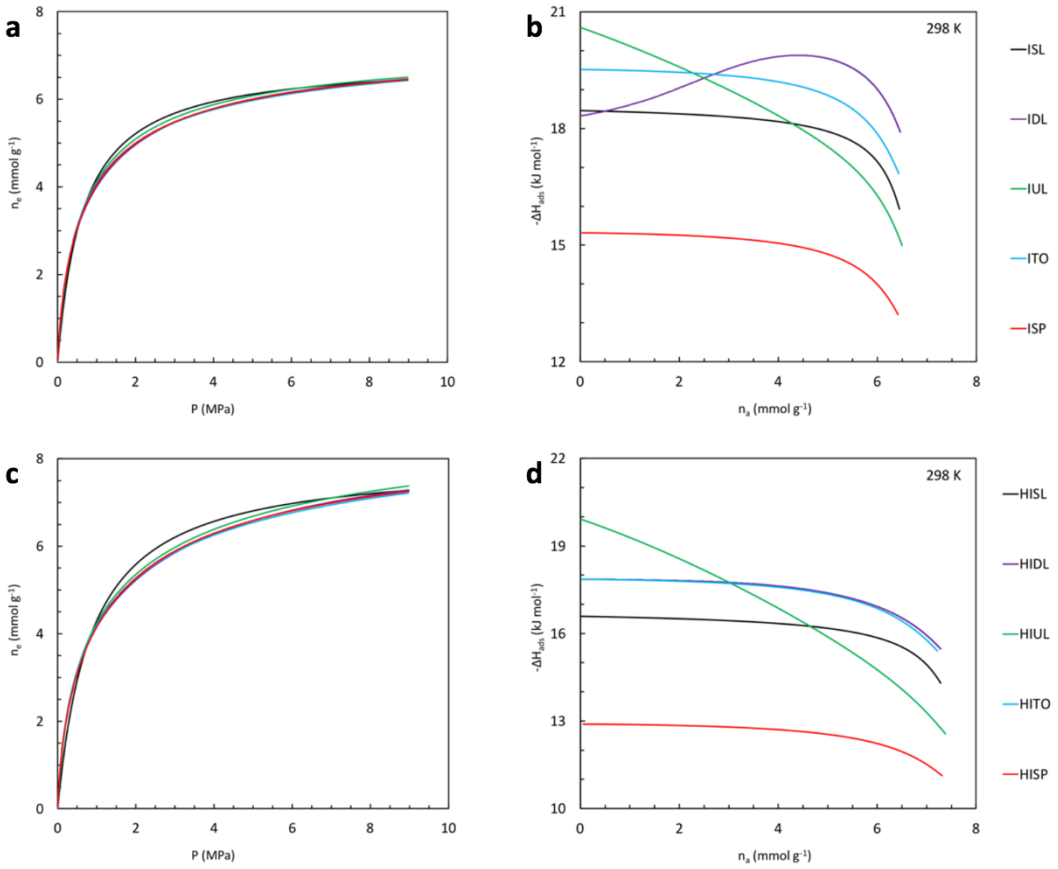

Figure 9. (a) Fitted excess adsorption uptake of methane on CNS-201 (uncorrected for helium adsorption) between 0.01-9 MPa at 298 K, assuming zero adsorbed phase volume. (b) Isoexcess heat of adsorption of methane on CNS-201 as a function of excess adsorption between 0.01-9 MPa at 298 K, calculated by fifteen different models, and compared to the "middle regime" of the isosteric results. (c) Fitted excess adsorption uptake of methane on CNS-201 (corrected for helium adsorption) between 0.01-9 MPa at 298 K, assuming zero adsorbed phase volume. (d) Isoexcess heat of adsorption of methane on CNS-201 as a function of excess adsorption between 0.01-9 MPa at 298 K, calculated by fifteen different models, and compared to the "middle regime" of the isosteric results.

Table 4. Best fit parameters and figures of assessment for adsorption of methane on CNS-201 between 247-526 K and 0.01-9 MPa for isoexcess heat of adsorption calculations.

		Isoexcess Model Uncorrected $V_a = 0$	Isoexcess Model Helium-Corrected $V_a = 0$	Units
Langmuir (ISL)	n_{max}	6.910	7.971	mmol g^{-1}
	A	0.000896	0.00145	MPa^{-1}
	E	18.456	16.586	kJ mol^{-1}
	RSS pt^{-1}	0.082	0.083	mmol g^{-1} pt^{-1}
	R_a^2	0.983	0.986	mmol g^{-1} pt^{-1}
Dual-Site Langmuir (IDL)	n_{max}	7.203	8.642	mmol g^{-1}
	α	0.383	0.411	unitless
	A_1	0.000125	0.000241	MPa^{-1}
	E_1	21.048	17.940	kJ mol^{-1}
	A_2	0.00395	0.00318	MPa^{-1}
	E_2	17.803	17.854	kJ mol^{-1}
	RSS pt^{-1}	0.261	0.0471	mmol g^{-1} pt^{-1}
	R_a^2	0.991	0.999	mmol g^{-1} pt^{-1}
Unilan (IUL)	n_{max}	7.194	8.891	mmol g^{-1}
	ΔS	-9.550	-9.187	R
	E_{min}	14.943	11.261	kJ mol^{-1}
	E_{max}	22.723	22.265	kJ mol^{-1}
	RSS pt^{-1}	0.263	0.095	mmol g^{-1} pt^{-1}
	R_a^2	0.986	0.996	mmol g^{-1} pt^{-1}

* - "RSS pt^{-1}" refers to the residual sum of squares, per fitted point

** - molar, volume, and pressure quantities in this table refer to CH_4, and per gram quantities refer to the mass of adsorbent (CNS-201)

		Isoexcess Model Uncorrected $V_a = 0$	Isoexcess Model Helium-Corrected $V_a = 0$	Units
Tóth (ITO)	n_{max}	7.573	9.490	mmol g^{-1}
	A	0.00981	0.00183	MPa^{-1}
	E	19.520	17.856	kJ mol^{-1}
	t	0.680	0.572	unitless
	RSS pt^{-1}	0.207	0.009	mmol g^{-1} pt^{-1}
	R_a^2	0.989	0.998	mmol g^{-1} pt^{-1}
Sips (ISP)	n_{max}	7.414	8.981	mmol g^{-1}
	A	0.00249	0.00474	MPa^{-1}
	E	15.320	12.894	kJ mol^{-1}
	m	1.282	1.387	unitless
	RSS pt^{-1}	0.196	0.041	mmol g^{-1} pt^{-1}
	R_a^2	0.990	0.998	mmol g^{-1} pt^{-1}

* - "RSS pt^{-1}" refers to the residual sum of squares, per fitted point

** - molar, volume, and pressure quantities in this table refer to CH_4, and per gram quantities refer to the mass of adsorbent (CNS-201)

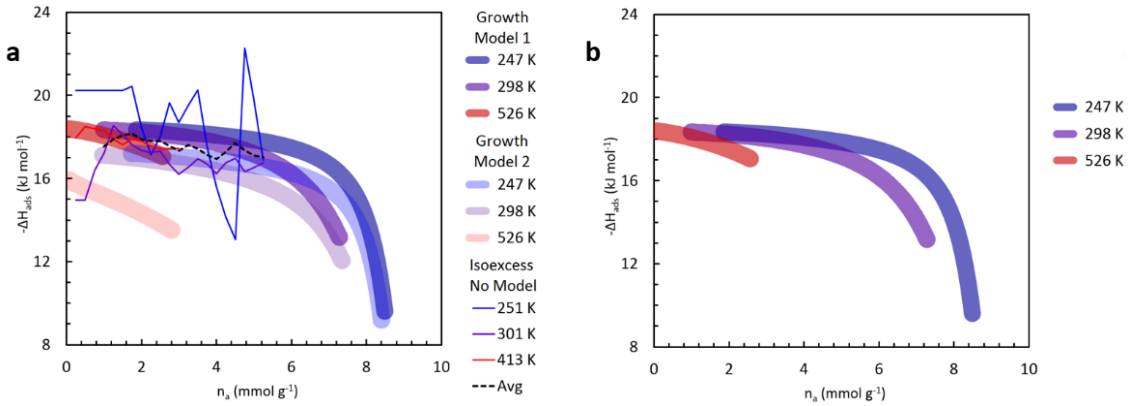

Figure 10. (a) Isosteric heat of adsorption of methane on CNS-201, comparing the "high heat" (SL1, DL1, TO1, and SP1) and "low heat" (SL2-3, DL2-3, TO2-3, and SP2-3) results to those obtained by a modeless isoexcess approach (HINA). (b) Final assessment of the enthalpy of adsorption of methane on CNS-201 as a function of adsorbed amount and temperature between 247-526 K.

CHAPTER FOUR

DISCUSSION

Fifteen different models were fitted to measured excess adsorption equilibria of methane on a microporous activated carbon, CNS-201, to assess the role of the model type, adsorbed phase growth behavior, and suggested "correction" for errors due to improper skeletal density measurement on calculations of the enthalpy of adsorption. It should be noted that in numerous reports describing the fitting of adsorption equilibria, each isotherm (at T_i) is fitted individually, leading to the accumulation of $N \times i$ independent fitting parameters (e.g., leading to 24 unique parameters for a set of 6 isotherms modeled using the Tóth equation[51]). In many such cases, the true number of independent fitting parameters used is not often clear; in this work, we emphasize that accurate fitment over the entire dataset *globally* for a single material is the criterion of comparison. Three important results of the fitting efforts alone are:

(a) the uncorrected adsorption equilibria (which do not acknowledge any significant error imparted by helium void volume determination at ambient temperature) are accurately fitted by all absolute adsorption models employed herein except for the single-site Langmuir models (see Figure 5) and yield physically reasonable values for the parameters n_{max} and V_{max},

(b) the helium adsorption "corrected" adsorption equilibria (modified as recommended elsewhere[35]) are accurately fitted by all absolute adsorption

models employed herein except for the single-site Langmuir models (see Figure 6) but do not yield physically reasonable values for the parameters n_{max} and V_{max} (leading to unphysically dense packing of methane molecules within the volume allotted to adsorption above the surface of CNS-201), and

(c) the helium adsorption "corrected" adsorption equilibria are also accurately fitted by all of the excess adsorption models employed herein (which accept the approximation that $n_e \approx n_a$) yielding reasonable values for the parameter n_{max} but no insight into the volume of the adsorbed phase (which is taken by definition to be zero).

The above results permit the ruling out of fitting the helium adsorption corrected adsorption equilibria with any model that adequately acknowledges the fundamental concept of the excess quantity of adsorption identified by Gibbs (i.e., which acknowledges that $n_e \neq n_a$). We find this to be a disqualifying factor for the utility of the proposed helium adsorption correction; rather, fitting of the as-measured ("uncorrected") adsorption equilibria to absolute adsorption models yields best fit parameters with physical meaningfulness (especially in the case of DL1 and TO1). The likely cause of this effect is the absence of an excess adsorption maximum in all isotherms after the "correction" has been applied, leading to an unphysically low volume attributed to the adsorbed phase. This result is not unique to CNS-201, and implies that the "correction" imparted by Equation 21 while supported by evidence as to the non-negligible adsorption of helium on porous carbon materials,[35] is perhaps an overcompensation for those effects. We note

that the presence of the Gibbs excess maximum in high-pressure supercritical adsorption equilibria is not disputed, even when helium adsorption is considered as a potential source of error.[52, 53]

Employing different approximations as to the growth of the adsorbed phase volume (Growth Models 1-3) leads to several consistent trends; most importantly, Growth Model 1 leads to a consistently higher estimated heat of adsorption than those of Growth Models 2 and 3, which yield similar results. Hence it is a result of the present work that:

(a) the assumption of a Growth Model 1 type absolute adsorption equation may lead to an overestimation of the isosteric heat of adsorption, and

(b) the assumption of a Growth Model 2 type absolute adsorption equation may lead to an underestimation of the isosteric heat of adsorption.

In Growth Model 1, the absolute volume ascribed to the adsorbed phase increases as adsorption progresses, a physically reasonable suggestion. For simplicity, a constant amount of volume (the adsorbate molar volume, v_a) is imparted per mole of adsorbate. This is an overly simplistic assumption since the molar volume of the adsorbed phase cannot possibly be identical across the entire phase diagram; nevertheless, it is an often employed assumption in other work.[54-56] An additional pitfall of this assumption is that at low quantities of adsorption, a significant volume of the pore space of the microporous material is ascribed as being part of the “bulk” fluid despite its rather un-bulk-like characteristics. This issue is lessened in consideration of the low bulk pressures under these

circumstances, corresponding to rather few “bulk fluid” molecules being considered as inhabiting the inner pore structure without being adsorbed.

Growth Model 2 fixes the adsorbed phase volume as constant throughout the entirety of adsorption; the density of the adsorbed phase therefore starts out negligibly low, and then increases as adsorption takes place, up to a maximum. This is also a physically unrealistic model unless it must be accepted that molecules in the bulk fluid cannot enter the pore system except by adsorption. It is also notable that there is no dependence on temperature in this model, so that at high temperatures the adsorbed phase density is *always* taken to be very (if not negligibly) low. This type of adsorbed phase volume growth model is often employed in other work.[57, 58]

Growth Model 3 was developed herein to serve as an intermediate model between the aforementioned Growth Model 1 and Growth Model 2. In this case, the absolute volume of the adsorbed phase grows upon the addition of molecules to it (as in Growth Model 1), but is not necessarily 1:1 correlated in terms of volume per mole added. For simplicity, a volume growth of the adsorbed phase was taken as proportional to a simple Langmuir equation (regardless and independent of the type of adsorption model employed to determine the amount adsorbed as a function of pressure and temperature). Growth Model 3 therefore adds an additional parameter to the overall fitting equation, resulting in $N = 5$ for SL3, $N = 6$ for UL3, SP3, and TO3, and $N = 8$ for DL3. In the analysis performed herein, none of the models employing Growth Model 3 could be justified in light of the undesired

complexity of the additional independent fitting parameter (resulting in only similar or lower values of R_a^2 to other models).

To circumvent any reliance on the growth of the adsorbed phase in calculating thermodynamic quantities, the isoexcess method has been suggested.[44-46] While enticing, we find herein that both the model-based and modeless approaches to the isoexcess method lead to even less agreement in the calculated enthalpy of adsorption that that determined by the isosteric method. Nevertheless, the isoexcess heats of adsorption (Figure 9), and the modeless approach in particular (Figure 10), serve as a useful benchmark for the accuracy of the isosteric approach (Figure 7). The disparity between the "high heat" and the "low heat" results in the isosteric method can be reconciled by comparison with the modeless isoexcess heat of adsorption. In this way, the high heat result is determined to be more accurate in this work, hence encouraging the use of DL1 and TO1 as appropriate fitting equations for modelling supercritical methane adsorption on microporous carbon materials. This analysis is shown in Figure 10a. Similar conclusions can be drawn about the thermodynamics of methane adsorption on wider pore microporous carbon materials such as MSC-30 and ZTC. The best practices in obtaining physically reasonable and model-independent thermodynamic results are to employ a multiplicity of adsorption models and place larger error bars on the quantities estimated, as shown in Figure 10b. This presentation of the thermodynamic results lends meaningful insight into the

behavior of the adsorbed phase as a function of temperature and adsorbed quantity while acknowledging the limited precision of the isosteric method.

CHAPTER FIVE

CONCLUSIONS AND FUTURE WORK

Methodological experiments were carried out to elucidate the effects of various aspects of the adsorption isosteric method for the determination of the enthalpy of adsorption. The case of primary study is the supercritical adsorption of methane on exclusively microporous activated carbon, a well-characterized material known as CNS-201. Three main considerations were the role of the fitting model (and its inherent characteristics), the treatment of the growth of the adsorbed phase volume with adsorption, and the acknowledgement of the difference between absolute and excess adsorption (including employing the "isoexcess" method for comparison to the isosteric method). The nature of the fitting model chosen played a significant role in the resulting calculations of the enthalpy of adsorption, within both the isosteric and isoexcess approaches. A modeless approach can also be used, but the results are far less informative as to temperature and site occupancy dependencies. In addition, the growth of the adsorbed phase as adsorption increases plays a very significant role that is not often considered; Growth Models 1 and 2, the most commonly employed approximations, yield enthalpies of adsorption that differ by ~2 kJ mol^{-1}, a ~10-15% effect in the present work. While the physical picture of both growth model types is flawed, that associated with Growth Model 1 is more reasonable and is also statistically justified in the work presented herein. In conclusion, we recommend a multi-model approach to assessing the enthalpy of

adsorption based on measured adsorption equilibria, and most importantly, the collection of copious experimental data, especially in the region beyond the Gibbs excess maximum.

It is recommended that equilibrium helium adsorption isotherms are measured for CNS-201, between 238-526 K and 0.01-9 MPa and analyzed using the uncorrected procedure described in this work. The results from this future work will provide insight on the significance of the potential error introduced from the determination of the void volume via helium and how it impacts the thermodynamic properties. Furthermore, this study will either validate or refine the results for the helium corrected data presented in this work.

REFERENCES CITED

1. Bolisetty, S. and M. Raffaele, *Amyloid-carbon hybrid membranes for universal water purification.* Nat. Nanotechnol., 2016. **11**: p. 365-371.

2. Wang, L. and X. Hu, *Recent advances in porous carbon materials for electrochemical energy storage.* Chem. Asian J., 2018. **13**: p. 1518-1529.

3. Gadipelli, S. and Z.X. Guo, *Graphene-based materails: Synthesis and gas sorption, storage, and separation.* Prog. Mater. Sci., 2015. **69**: p. 1-60.

4. Rouquerol, J., et al., *Recommendations for the characterization of porous solids.* Pure & Appl. Chem., 1994. **66**(8): p. 1739-1758.

5. Presser, V., M. Heon, and Y. Gogotsi, *Carbide-derived carbons- from porous networks to nanotubes and graphene.* Advanced Functional Materials, 2011. **21**: p. 810-833.

6. Gogotsi, Y., et al., *Importance of pore size in high-pressure hydrogen storage by porous carbons.* Int. J. Hydrog. Energy, 2009. **34**: p. 6314-6319.

7. Makal, T.A., et al., *Methane storage in advanced porous materials.* Chem. Soc. Rev., 2012. **41**: p. 7761-7779.

8. Lee, J. and J. Kim, *Recent progress in the synthesis of porous carbon materials.* Adv. Mater., 2006. **18**: p. 2073-2094.

9. Nishihara, H. and T. Kyotani, *Zeolite-templated carbons - three-dimensional microporous graphene frameworks.* Chem. Commun., 2018. **54**: p. 5648-5673.

10. Welz, S., Y. Gogotsi, and M.J. McNallan, *Nucleation, growth, and graphitization of diamond nanocrystals during chlorination of carbides.* Applied Physics, 2003. **93**(7): p. 4207-4214.

11. Ariyanto, T., et al., *Controlled synthesis of core-shell carbide-derived carbons through in situ generated chlorine.* Carbon, 2017. **115**: p. 422-429.

12. Yushin, G. and A. Nikitin, *Chapter 8 carbide-derived carbon*, in *nanomaterials handbook*, Y. Gogotsi, Editor. 2006, Taylor & Francis Group.

13. Remington, E.L., et al., *Novel approach to the formation of carbide-dervied carbons using NH4Cl*, in *233rd Electrochemical Society Meeting* 2018: Seattle, WA.

14. Stadie, N.P., *Synthesis and thermodynamic studies of physisorptive energy storage materials*. 2013, California Institute of Technology.

15. Inagaki, M., *Pores in carbon materials-importance of their control.* New Carbon Materials, 2009. **24**(3): p. 193-232.

16. Terranova, M.L., S. Orlanducci, and M. Rossi, *Carbon nanomaterials for gas adsorption*. 2013, Singapore: Pan Standford Publishing Pte. Ltd. .

17. Nugent, P., et al., *Porous materials with optimal adsorption thermodynamics and kinetics for CO2 separation.* Nature, 2013. **495**(7439): p. 80.

18. Shekhah, O., et al., *Made-to-order metal-organic frameworks for trace carbon dioxide removal and air capture.* Nature communications, 2014. **5**: p. 4228.

19. Cui, X., et al., *Pore chemistry and size control in hybrid porous materials for acetylene capture from ethylene.* Science, 2016. **353**(6295): p. 141-144.

20. Bhatia, S.K. and A.L. Myers, *Optimum conditions for adsorptive storage.* Langmuir, 2006. **22**: p. 1688-1700.

21. Foo, K.Y. and B.H. Hameed, *Insights into the modeling of adsorption isotherm systems.* Chemical engineering journal, 2010. **156**(1): p. 2-10.

22. Langmuir, I., *The adsorption of gases on plane surfaces of glass, mica and platinum.* J. Am. Chem. Soc., 1918. **40**(9): p. 1361-1403.

23. Stadie, N.P., et al., *Anomalous isosteric enthalpy of adsorption of methane on zeolite-templated carbon.* J. Am. Chem. Soc., 2013. **135**(3): p. 990-993.

24. Stadie, N.P., et al., *Unusual entropy of adsorbed methane on zeolite-templated carbon.* J. Phys. Chem. C, 2015. **119**(47): p. 26409-26421.

25. Tóth, J., *Gas-(Dampf-)adsorption an festen Oberflächen inhomogener Aktivität. III.* Acta Chimica Academiae Scientarium Hungaricae, 1962. **32**(1).

26. Halsey, G. and H.S. Taylor, *The adsorption of hydrogen on tungsten powders.* The journal of chemical physics, 1947. **15**(9): p. 624-630.

27. Sips, R., *On the structure of a catalyst surface.* The Journal of Chemical Physics, 1948. **16**(5): p. 490-495.

28. Sips, R., *On the structure of a catalyst surface. II.* The Journal of Chemical Physics, 1950. **18**(8): p. 1024-1026.

29. Stadie, N.P., et al., *Zeolite-templated carbon materials for high-pressure hydrogen storage.* Langmuir, 2012. **28**: p. 10057-10063.

30. Bénard, P. and R. Chahine, *Modeling of high-pressure adsorption isotherms above the critical temperature on microporous adsorbents: application to methane.* Langmuir, 1997. **13**: p. 808-813.

31. Okambawa, R., et al., *Gas− Solid interaction and the virial description of the adsorption of methane on steam-activated carbon.* Langmuir, 2000. **16**(3): p. 1163-1166.

32. Purewal, J.J., et al., *Pore size distribution and supercritical hydrogen adsorption in activated carbon fibers.* Nanotechnology, 2009. **20**(20): p. 204012.

33. Li, Y. and R.T. Yang, *Hydrogen storage on platinum nanoparticles doped on superactivated carbon.* The Journal of Physical Chemistry C, 2007. **111**(29): p. 11086-11094.

34. Nishihara, H. and T. Kyotani, *Zeolite-templated carbons - three-dimensional microporous graphene frameworks.* Chemical Communications, 2018. **54**: p. 5648-5673.

35. Sircar, S., *Role of helium void measurement in estimation of Gibbsian surface excess.* Proceedings of Fundamental of Adsorption, 2002. **7**: p. 656-663.

36. Bell, I.H., et al., *Pure and pseudo-pure fluid thermophysical property evaluation and the open-source thermophysical property library CoolProp.* Industrial & engineering chemistry research, 2014. **53**(6): p. 2498-2508.

37. Kvalseth, T.O., *Cautionary note about R2.* The American Statistician, 1985. **39**(4): p. 279-285.

38. Lemmon, E.W., M.L. Huber, and M.O. McLinden, *NIST standard reference database 23: reference fluid thermodynamic and transport properties − REFPROP*. 2007. p. Number Version 8.0 in Standard Reference Data Program.

39. Honig, J. and L. Reyerson, *Adsorption of nitrogen, oxygen and argon on rutile at low temperatures; applicability of the concept of surface heterogeneity.* The Journal of Physical Chemistry, 1952. **56**(1): p. 140-144.

40. Swenson, H. and N.P. Stadie, *Langmuir.* Langmuir, 2019.

41. Tóth, J., *State equations of the solid gas interface layer.* Acta Chimica Academiae Scientarium Hungaricae, 1971. **69**(311).

42. Kumar, K.V., et al., *A site energy distribution function from Toth isotherm for adsorption of gases on heterogeneous surfaces.* Physical Chemistry Chemical Physics, 2011. **13**(13): p. 5753-5759.

43. Fernbacher, J.M. and L.A. Wenzel, *Adsorption equilibria at high pressures in the helium-nitrogen-activated carbon system.* Industrial & Engineering Chemistry Fundamentals, 1972. **11**(4): p. 457-465.

44. Sircar, S., *Gibbsian surface excess for gas adsorption – revisited.* Ind. Eng. Chem. Res., 1999. **38**: p. 3670-3682.

45. Sircar, S., et al., *Isosteric heat of adsorption: theory and experiment.* J. Phys. Chem. B, 1999. **103**: p. 6539-6546.

46. Sircar, S., *Comments on the artificiality of actual amount adsorbed.* Industrial & Engineering Chemistry Research, 2018. **57**(19): p. 6766-6773.

47. Stadie, N.P., *Synthesis and thermodynamic studies of physisorptive energy storage materials*. 2013, California Institute of Technology: California Institute of Technology.

48. Sircar, S., *The genius of Gibbsian surface excess (GSE) framework for fluid (gas or liquid)–Solid adsorption: A powerful practical tool.* Separation and Purification Technology, 2019. **213**: p. 235-245.

49. Do, D.D. and H.D. Do, *Adsorption of supercritical fluids in non-porous and porous carbons: analysis of adsorbed phase volume and density.* Carbon, 2003. **41**(9): p. 1777-1791.

50. Rouquerol, F., J. Rouquerol, and K.S.W. Sing, *Adsorption by powders and porous solids: principles, methodology, and applications*. 1999, San Diego: Academic Press. xvi, 467 p.

51. Bimbo, N., et al., *Isosteric enthalpies for hydrogen adsorbed on nanoporous materials at high pressures.* Adsorption, 2014. **20**: p. 373-384.

52. Malbrunot, P., et al., *Adsorbent helium density measurement and its effect on adsorption isotherms at high pressure.* Langmuir, 1997. **13**(3): p. 539-544.

53. Herbst, A. and P. Harting, *Thermodynamic description of excess isotherms in high-pressure adsorption of methane, argon and nitrogen.* Adsorption, 2002. **8**(2): p. 111-123.

54. Dreisbach, F., R. Staudt, and J.U. Keller, *High pressure adsorption data of methane, nitrogen, carbon dioxide and their binary and ternary mixtures on activated carbon.* Adsorption, 1999. **5**(3): p. 215-227.

55. Krooss, B.M., et al., *High-pressure methane and carbon dioxide adsorption on dry and mosture-equilibriated Pennsylvanian coals.* Int. J. Coal Geol. , 2002. **51**(2): p. 69-92.

56. Agarwal, R.K. and J.A. Schwarz, *Analysis of high pressure adsorption of gases on activated carbon by potential theory.* Carbon, 1988. **26**(6): p. 873-887.

57. Purewal, J., et al., *Improved hydrogen storage and thermal conductivity in high-density MOF-5 composites.* The Journal of Physical Chemistry C, 2012. **116**(38): p. 20199-20212.

58. Bae, J.-S. and S.K. Bhatia, *High-pressure adsorption of methane and carbon dioxide on coal.* Energy & Fuels, 2006. **20**(6): p. 2599-2607.

APPENDIX

Once the adsorption data are fitted using one of the global adsorption models (yielding a single set of independent fitting parameters across the entire temperature and pressure range of interest), the thermodynamics calculations are carried out in the same way for each model. In the standard case (referred to herein as the "isosteric method"), the calculation of the difference in molar entropy between the adsorbed phase and the bulk fluid (the isosteric entropy of adsorption, ΔS_{ads}) is performed using the completely general Clapeyron equation:

$$\left(\frac{\partial P}{\partial T}\right)_{n_a} = \frac{\Delta S_{ads}}{\Delta v_{ads}} = \frac{S_a - S_g}{v_a - v_g}$$

where S is molar entropy, v is molar volume, T is temperature, and P is pressure. The subscripts indicate either the adsorbed phase (a), the bulk fluid (g), or the difference between these phases (ads, indicating the transition from g to a). This completely general equation is applicable to any two phases in thermal and mechanical equilibrium (i.e., at the same temperature and pressure). Rearranged:

$$\Delta S_{ads} = \left(v_a - v_g\right)\left(\frac{\partial P}{\partial T}\right)_{n_a}$$

At equilibrium at constant temperature and pressure (i.e., when $\Delta G_{ads} = 0$), the isosteric enthalpy of adsorption, ΔH_{ads}, is directly related to the isosteric entropy of adsorption as follows:

$$T\Delta S_{ads} = \Delta H_{ads} = T\left(v_a - v_g\right)\left(\frac{\partial P}{\partial T}\right)_{n_a}$$

The parts of the above equation required to calculate ΔH_{ads} are determined as follows:

Quantity	Method of Determination
T, P	specified
$v_a(T, P)$	modeled, by applying Growth Model 1, 2, or 3
$v_g(T, P)$	extracted from the NIST Refprop database
$\left(\frac{\partial P}{\partial T}\right)_{n_a}(T, P)$	modeled, by applying the adsorption equation

For the three Growth Models employed in this work, the molar volume of the adsorbed phase, v_a, is calculated as follows:

Adsorbed Phase Molar Volume	Growth Model
$v_a = \frac{V_{max}}{n_{max}}$	Growth Model 1
$v_a(T, P) = \frac{V_{max}}{n_a(T, P)}$	Growth Model 2
$v_a(T, P) = V_{max}\frac{\theta_{growth}(T, P)}{n_a(T, P)}$	Growth Model 3

Regardless of the adsorption model used, Growth Model 3 is always dependent upon an additional parameter referred to as K_{growth}. This represents an arbitrary monotonic growth of the adsorbed phase as a function of increased

pressure, an intermediate model between that of constant adsorbed phase growth (as in Growth Model 1) and constant adsorbed phase volume (as in Growth Model 2).

For each of the five main adsorption models used in this work, the derivative of pressure with respect to temperature must be calculated analytically as a function of temperature, pressure, and the various independent fitting parameters associated with each model. To simplify, the derivative is first rewritten as a constant occupancy isostere by recognizing the two as equivalent quantities (since $n_a \propto \theta$):

$$\left(\frac{\partial P}{\partial T}\right)_{n_a} = \left(\frac{\partial P}{\partial T}\right)_{\theta}$$

The following (cyclic) rearrangement is then performed:

$$\left(\frac{\partial P}{\partial T}\right)_{\theta} = -\left(\frac{\partial P}{\partial \theta}\right)_{T}\left(\frac{\partial \theta}{\partial T}\right)_{P}$$

$$\left(\frac{\partial P}{\partial T}\right)_{\theta} = -\left(\frac{\partial \theta}{\partial P}\right)_{T}^{-1}\left(\frac{\partial \theta}{\partial T}\right)_{P}$$

The two quantities needed are the first partial derivatives of the adsorption site occupancy with respect to pressure and temperature. These expressions are unique to each adsorption equation and all have analytical solutions, as derived below.

(Single-Site) Langmuir Equation (SL):

$$\theta(T,P) = \frac{KP}{1+KP}$$
$$K(T) = A\, e^{\frac{-E}{RT}}$$

$$\left(\frac{\partial\theta}{\partial P}\right)_T = \frac{(1+KP)K - KP(K)}{(1+KP)^2} = \frac{K}{(1+KP)^2}$$

$$\left(\frac{\partial\theta}{\partial T}\right)_P = \left(\frac{\partial\theta}{\partial K}\right)_P \left(\frac{\partial K}{\partial T}\right)_P = \left(\frac{(1+KP)P - KP(P)}{(1+KP)^2}\right)\left(\frac{EK}{RT^2}\right) = \left(\frac{P}{(1+KP)^2}\right)\left(\frac{EK}{RT^2}\right)$$

$$\left(\frac{\partial P}{\partial T}\right)_\theta = \frac{(1+KP)^2}{K}\left(\frac{P}{(1+KP)^2}\right)\left(\frac{EK}{RT^2}\right) = \frac{P}{K}\left(\frac{EK}{RT^2}\right) = \frac{PE}{RT^2}$$

Growth Model 1 (SL1):

$$\Delta H_{ads} = \left(\frac{V_{max}}{n_{max}} - \nu_g\right)\frac{PE}{RT}$$

Growth Model 2 (SL2):

$$\Delta H_{ads} = \left(\frac{V_{max}(1+PK)}{n_{max}PK} - \nu_g\right)\frac{PE}{RT}$$

Growth Model 3 (SL3):

$$\Delta H_{ads} = \left(\frac{V_{max}K_{growth}P(1+PK)}{n_{max}PK\left(1+PK_{growth}\right)} - \nu_g\right)\frac{PE}{RT}$$

Dual-Site Langmuir Equation (DL):

$$\theta(T,P) = (1-\alpha)\left(\frac{K_1 P}{1+K_1 P}\right) + \alpha\left(\frac{K_2 P}{1+K_2 P}\right)$$

$$K_1(T) = A_1\, e^{\frac{-E_1}{RT}} \qquad K_2(T) = A_2\, e^{\frac{-E_2}{RT}}$$

$$\left(\frac{\partial\theta}{\partial P}\right)_T = (1-\alpha)\left(\frac{K_1}{(1+K_1P)^2}\right) + \alpha\left(\frac{K_2}{(1+K_2P)^2}\right)$$

$$\left(\frac{\partial\theta}{\partial T}\right)_P = \left(\frac{\partial\theta}{\partial K_1}\right)_P \left(\frac{\partial K_1}{\partial T}\right)_P + \left(\frac{\partial\theta}{\partial K_2}\right)_P \left(\frac{\partial K_2}{\partial T}\right)_P$$
$$= (1-\alpha)\left(\frac{P}{(1+K_1P)^2}\right)\left(\frac{E_1K_1}{RT^2}\right) + \alpha\left(\frac{P}{(1+K_2P)^2}\right)\left(\frac{E_2K_2}{RT^2}\right)$$

$$\left(\frac{\partial P}{\partial T}\right)_\theta = \left((1-\alpha)\left(\frac{K_1}{(1+K_1P)^2}\right) + \alpha\left(\frac{K_2}{(1+K_2P)^2}\right)\right)^{-1}$$
$$\left((1-\alpha)\left(\frac{P}{(1+K_1P)^2}\right)\left(\frac{E_1K_1}{RT^2}\right) + \alpha\left(\frac{P}{(1+K_2P)^2}\right)\left(\frac{E_2K_2}{RT^2}\right)\right)$$

Growth Model 1 (DL1):

$$\Delta H_{ads} = T\left(\frac{V_{max}}{n_{max}} - v_g\right)$$
$$\left((1-\alpha)\left(\frac{K_1}{(1+K_1P)^2}\right) + \alpha\left(\frac{K_2}{(1+K_2P)^2}\right)\right)^{-1}$$
$$\left((1-\alpha)\left(\frac{P}{(1+K_1P)^2}\right)\left(\frac{E_1K_1}{RT^2}\right) + \alpha\left(\frac{P}{(1+K_2P)^2}\right)\left(\frac{E_2K_2}{RT^2}\right)\right)$$

Growth Model 2 (DL2):

$$\Delta H_{ads} = T\left(\frac{V_{max}}{n_{max}}\left(\frac{1+K_1P}{(1-\alpha)K_1P} + \frac{1+K_2P}{\alpha K_2P}\right) - v_g\right)$$
$$\left((1-\alpha)\left(\frac{K_1}{(1+K_1P)^2}\right) + \alpha\left(\frac{K_2}{(1+K_2P)^2}\right)\right)^{-1}$$
$$\left((1-\alpha)\left(\frac{P}{(1+K_1P)^2}\right)\left(\frac{E_1K_1}{RT^2}\right) + \alpha\left(\frac{P}{(1+K_2P)^2}\right)\left(\frac{E_2K_2}{RT^2}\right)\right)$$

Growth Model 3 (DL3):

$$\Delta H_{ads} = T\left(\frac{V_{max}}{n_{max}}\left(\frac{1+K_1P}{(1-\alpha)K_1P}+\frac{1+K_2P}{\alpha K_2P}\right)\left(\frac{K_{growth}P}{1+K_{growth}P}\right)-v_g\right)$$
$$\left((1-\alpha)\left(\frac{K_1}{(1+K_1P)^2}\right)+\alpha\left(\frac{K_2}{(1+K_2P)^2}\right)\right)^{-1}$$
$$\left((1-\alpha)\left(\frac{P}{(1+K_1P)^2}\right)\left(\frac{E_1K_1}{RT^2}\right)+\alpha\left(\frac{P}{(1+K_2P)^2}\right)\left(\frac{E_2K_2}{RT^2}\right)\right)$$

Unilan Equation (UL):

Note: pressure is in units of bar for Unilan model only.

$$\theta(T,P) = \frac{RT}{E_{max} - E_{min}} ln\left(\frac{a + Pe^{\frac{E_{max}}{RT}}}{a + Pe^{\frac{E_{min}}{RT}}}\right)$$

$$a = e^{\left(\frac{-\Delta S}{R}\right)}$$

$$\left(\frac{\partial\theta}{\partial P}\right)_T = \frac{aRT\left(e^{\frac{E_{max}}{RT}} - e^{\frac{E_{min}}{RT}}\right)}{(E_{max} - E_{min})\left(Pe^{\frac{E_{min}}{RT}} + a\right)\left(Pe^{\frac{E_{max}}{RT}} + a\right)}$$

$$\left(\frac{\partial\theta}{\partial T}\right)_P = \frac{PT\left(\left((PE_{max} - PE_{min})e^{\frac{E_{min}}{RT}} + aE_{max}\right)e^{\frac{E_{max}}{RT}} - aE_{min}e^{\frac{E_{min}}{RT}}\right)}{(E_{max} - E_{min})T^2\left(Pe^{\frac{E_{min}}{RT}} + a\right)\left(Pe^{\frac{E_{max}}{RT}} + a\right)}$$

$$\left(\frac{\partial \mathrm{P}}{\partial \mathrm{T}}\right)_\theta = \left(\frac{aRT\left(e^{\frac{E_{max}}{RT}} - e^{\frac{E_{min}}{RT}}\right)}{(E_{max} - E_{min})\left(Pe^{\frac{E_{min}}{RT}} + a\right)\left(Pe^{\frac{E_{max}}{RT}} + a\right)}\right)^{-1}$$

$$\left(\frac{PT\left(\left((PE_{max} - PE_{min})e^{\frac{E_{min}}{RT}} + aE_{max}\right)e^{\frac{E_{max}}{RT}} - aE_{min}e^{\frac{E_{min}}{RT}}\right)}{(E_{max} - E_{min})T^2\left(Pe^{\frac{E_{min}}{RT}} + a\right)\left(Pe^{\frac{E_{max}}{RT}} + a\right)}\right)$$

Growth Model 1 (UL1):

$$\Delta H_{ads} = \left(\frac{V_{max}}{n_{max}} - v_g\right) \left(\frac{aRT\left(e^{\frac{E_{max}}{RT}} - e^{\frac{E_{min}}{RT}}\right)}{(E_{max} - E_{min})\left(Pe^{\frac{E_{min}}{RT}} + a\right)\left(Pe^{\frac{E_{max}}{RT}} + a\right)}\right)^{-1} \left(\frac{PT\left(\left((PE_{max} - PE_{min})e^{\frac{E_{min}}{RT}} + aE_{max}\right)e^{\frac{E_{max}}{RT}} - aE_{min}e^{\frac{E_{min}}{RT}}\right)}{(E_{max} - E_{min})T^2\left(Pe^{\frac{E_{min}}{RT}} + a\right)\left(Pe^{\frac{E_{max}}{RT}} + a\right)}\right)$$

Growth Model 2 (UL2):

$$\Delta H_{ads} = \left(\frac{V_{max}}{n_{max}}\left(\frac{RT}{E_{min} - E_{max}} ln\left(\frac{a + Pe^{\frac{E_{max}}{RT}}}{a + Pe^{\frac{E_{min}}{RT}}}\right)\right)^{-1} - v_g\right) \left(\frac{aRT\left(e^{\frac{E_{max}}{RT}} - e^{\frac{E_{min}}{RT}}\right)}{(E_{max} - E_{min})\left(Pe^{\frac{E_{min}}{RT}} + a\right)\left(Pe^{\frac{E_{max}}{RT}} + a\right)}\right)^{-1} \left(\frac{PT\left(\left((PE_{max} - PE_{min})e^{\frac{E_{min}}{RT}} + aE_{max}\right)e^{\frac{E_{max}}{RT}} - aE_{min}e^{\frac{E_{min}}{RT}}\right)}{(E_{max} - E_{min})T^2\left(Pe^{\frac{E_{min}}{RT}} + a\right)\left(Pe^{\frac{E_{max}}{RT}} + a\right)}\right)$$

Growth Model 3 (UL3):

$$\Delta H_{ads} = \left(\frac{V_{max}}{n_{max}} \left(\frac{RT}{E_{min} - E_{max}} ln \left(\frac{a + Pe^{\frac{E_{max}}{RT}}}{a + Pe^{\frac{E_{min}}{RT}}} \right) \right)^{-1} \left(\frac{K_{growth} P}{1 + K_{growth} P} \right) - v_g \right) \left(\frac{aRT \left(e^{\frac{E_{max}}{RT}} - e^{\frac{E_{min}}{RT}} \right)}{(E_{max} - E_{min}) \left(Pe^{\frac{E_{min}}{RT}} + a \right) \left(Pe^{\frac{E_{max}}{RT}} + a \right)} \right)^{-1} \left(\frac{PT \left(\left((PE_{max} - PE_{min}) e^{\frac{E_{min}}{RT}} + aE_{max} \right) e^{\frac{E_{max}}{RT}} - aE_{min} e^{\frac{E_{min}}{RT}} \right)}{(E_{max} - E_{min}) T^2 \left(Pe^{\frac{E_{min}}{RT}} + a \right) \left(Pe^{\frac{E_{max}}{RT}} + a \right)} \right)$$

Tóth Equation (TO):

$$\theta(T,P) = \frac{KP}{(1+(KP)^t)^{-1/t}}$$

$$K(T) = A\, e^{\frac{-E}{RT}}$$

$$\left(\frac{\partial\theta}{\partial P}\right)_T = K((KP)^t+1)^{\frac{-1}{t}-1}$$

$$\left(\frac{\partial\theta}{\partial T}\right)_P = \left(\frac{\partial\theta}{\partial K}\right)_P \left(\frac{\partial K}{\partial T}\right)_P = \left(P((KP)^t+1)^{\frac{-1}{t}-1}\right)\left(\frac{EK}{RT^2}\right)$$

$$\left(\frac{\partial P}{\partial T}\right)_\theta = \left(K((KP)^t+1)^{\frac{-1}{t}-1}\right)^{-1}\left(P((KP)^t+1)^{\frac{-1}{t}-1}\right)\left(\frac{EK}{RT^2}\right) = \frac{PE}{RT^2}$$

Growth Model 1 (TO1):

$$\Delta H_{ads} = \left(\frac{V_{max}}{n_{max}} - v_g\right)\frac{PE}{RT}$$

Growth Model 2 (TO2):

$$\Delta H_{ads} = \left(\frac{V_{max}}{n_{max}}\left(\frac{(1+(KP)^t)^{-1/t}}{KP}\right) - v_g\right)\frac{PE}{RT}$$

Growth Model 3 (TO3):

$$\Delta H_{ads} = \left(\frac{V_{max}}{n_{max}}\left(\frac{(1+(KP)^t)^{-1/t}}{KP}\right)\left(\frac{K_{growth}P}{1+K_{growth}P}\right) - v_g\right)\frac{PE}{RT}$$

Sips Equation (SP):

$$\theta(T,P) = \frac{(KP)^{1/m}}{1+(KP)^{1/m}}$$

$$K(T) = A\, e^{\frac{-E}{RT}}$$

$$\left(\frac{\partial\theta}{\partial P}\right)_T = \frac{\frac{1}{m}(KP)^{1/m}}{P\left(1+(KP)^{\frac{1}{m}}\right)^2}$$

$$\left(\frac{\partial\theta}{\partial T}\right)_P = \left(\frac{\partial\theta}{\partial K}\right)_P \left(\frac{\partial K}{\partial T}\right)_P = \left(\frac{\frac{1}{m}(KP)^{1/m}}{K(1+(KP)^{1/m})^2}\right)\left(\frac{EK}{RT^2}\right)$$

$$\left(\frac{\partial P}{\partial T}\right)_\theta = -\left(\frac{\frac{1}{m}(KP)^{1/m}}{P(1+(KP)^{1/m})^2}\right)^{-1}\left(\frac{\frac{1}{m}(KP)^{1/m}}{K(1+(KP)^{1/m})^2}\right)\left(\frac{EK}{RT^2}\right) = \frac{PE}{RT^2}$$

Growth Model 1 (SP1):

$$\Delta H_{ads} = \left(\frac{V_{max}}{n_{max}} - v_g\right)\frac{PE}{RT}$$

Growth Model 2 (SP2):

$$\Delta H_{ads} = \left(\frac{V_{max}}{n_{max}}\left(\frac{1+(KP)^{1/m}}{(KP)^{1/m}}\right) - v_g\right)\frac{PE}{RT}$$

Growth Model 3 (SP3):

$$\Delta H_{ads} = \left(\frac{V_{max}}{n_{max}}\left(\frac{1+(KP)^{1/m}}{(KP)^{1/m}}\right)\left(\frac{K_{growth}P}{1+K_{growth}P}\right) - v_g\right)\frac{PE}{RT}$$